University of Stavanger

Faculty of Science and Technology

MASTER'S THESIS

Study program/Specialization: Petroleum Geosciences Engineering	Spring, 2016 Open
Writer: Darjan Kundacina	(Writer's signature)
Faculty supervisor: Nestor Cardozo External supervisor: Lothar Schulte, Schlumberger SIS	
Title of thesis: Evaluation of strategies for fracture modeling: A case study at Teapot Dome, Wyoming	
Credits (ECTS): 30	
Keywords: Fracture modeling, Seismic attributes, Teapot Dome	Pages: 82 +enclosure: CD Stavanger, June 15, 2016

Evaluation of strategies for fracture modeling: A case study at Teapot Dome, Wyoming

by

Darjan Kundacina

Master Thesis

Presented to the Faculty of Science and Technology

The University of Stavanger

The University of Stavanger

June 2016

Acknowledgements

I am grateful to many people who provided me with support during my education and writing of the thesis. First, I would like to express my special gratitude to the advisors Lothar Schulte and Nestor Cardozo, for the guidance, patience and encouragement through the thesis project. I truly appreciate the immense help provided in form of constructive discussions, valuable comments and text editing that have helped improving my research skills and successfully completing my thesis.

I would like to extend my gratitude to the professors, stuff and classmates at the Department of Petroleum Engineering that made the last two years inspiring and enjoyable.

I would like to thank the Rocky Mountain Oilfield Testing Center (RMOTC) for providing the dataset used in the thesis. Also, thanks to Schlumberger for providing the Petrel license necessary for the successful completion of the thesis. Especially thanks to Andreas Habel for setting up the work station and IT support during the thesis work.

I sincerely thanks to my family and friends for their continued support and encouragement. Lastly, I would like to dedicate the work to my wife Ana and daughter Hana. Their infinite support, love and patience were crucial for the successful completion of my education and the master thesis.

Abstract

Evaluation of strategies for fracture modeling: A case study at Teapot Dome, Wyoming

Darjan Kundacina

The University of Stavanger, 2016

Supervisor: Nestor Cardozo

External Supervisor: Lothar Schulte

The characterization of fractured reservoirs is complex. Fracture modeling is often based on very limited well data and therefore is subject to high uncertainty. Typically, the standard modeling workflow uses interpolation algorithms to predict the fracture spatial distribution. This thesis shows an alternative workflow for improving fracture modeling between wells through the use of seismic attributes. The standard and the alternative workflows are applied to a public dataset from the Teapot Dome in central Wyoming, USA. The Teapot Dome is a basement-cored anticline above a thrust. The main objective of the thesis is to compare fracture models of the anticline guided by the two approaches: the standard interpolation based approach, and the seismic based approach using attributes sensitive to faults. The generated models differ mainly in the way of modeling the fracture intensity. The evaluation and uncertainty assessment of these techniques is based on the reservoir permeability derived from fracture models. A comparison of these two methods provides insight into the complexity and uncertainty involved in fracture modeling. In addition, the results show the disadvantages of models guided by the interpolation algorithms, Kriging and Gauss simulation. On the other hand, the seismic based workflow delivers fracture models that are more reliable. Although the seismic based fracture models give a similar permeability distribution like the interpolation methods, they show differences associated with the spatial distribution and connectivity of high permeability zones.

Table of Contents

List of Tables

List of Figures

1. Introduction

Natural fractured reservoirs (NFR) represent a considerable percentage of total hydrocarbon reservoirs in the world (Nelson, 2001). Compared to conventional reservoirs, NFR behave in significantly different manner and their characterization is far more complex. NFR can act as dual flow with presence of fluid flow in the matrix and the connected fractures. The presence of fractures and high flow zones within reservoirs lead to permeability anisotropy and heterogeneity. The flow through fractures often is greater than that through the tight matrix, and represents the main fluid path (Nelson, 2001; van der Most, 2008). Fractures form under the action of stress. The tectonic regime and orientation of paleo-stress decide on the fracture type (joint, shear fractures and stylolites) and fracture orientation (Fossen, 2010). Fracture modeling is a complex procedure of characterization and spatial prediction of fractures in order to the predict reservoir behavior. A reliable fracture model assumes a realistic representation of the fracture network at the reservoir level. Therefore, an accurate fracture characterization and a reliable fracture model are crucial for the reservoir simulation.

In general, at the reservoir level, well logs provide essential information regarding fractures. These data have validity in the close vicinity of the wells. Hence, fracture characterization requires additional efforts to extrapolate to areas away from the wells. While additional information for some parameters (length, aperture, orientation) are often obtained from outcrops and analogues, the largest uncertainty is related to the fracture intensity. The standard procedure in fracture modeling estimates the fracture intensity from the fractures intersecting the wells. Lorenz and Hill (1992) refer to the method of fracture counting on core data and emphasize the disadvantages of this technique. Furthermore, the standard procedure employs geostatistic methods to estimate fracture density throughout the model. Interpolation algorithms such as Kriging and Sequential Gaussian Simulation (SGS), frequently result in unsuccessful predictions of fracture distributions (El Ouahed et al., 2005). In case of limited well control, the fracture intensity distribution and hence the fracture model becomes unreliable. Consequently, fracture modeling requires additional guidance such as a reliable linkage of fracture intensity to regional or local tectonic events (Nelson, 2001; Stearns and Friedman, 1972; Zellou et al., 1995). Many authors have introduced

different techniques to guide fracture modeling such as the usage of seismic attributes (Chopra and Marfurt, 2007; Shen and Ouenes, 2003; Thachaparambil, 2015; Wilson et al., 2013), random regional stress field (Joonnekindt et al., 2013; Phillips et al., 2014), and neural network approach (Ouenes, 2000; Ouenes and Hartley, 2000; Ouenes et al., 1995; Zellou et al., 1995). These techniques have been applied to different datasets and areas, which makes it difficult to compare them and evaluate their advantages. The absence of a study that describes and compares the results of different fracture modeling workflows is one motivation of this thesis.

The Teapot Dome in central Wyoming (Figure 1) is an excellent example of a NFR. The Teapot Dome as part of the large Laramide complex is also well known as a Naval Petroleum Reserve (NPR3). Located near the southwestern margin of the Powder River basin, the Teapot Dome is an elongated, asymmetrical, basement-cored anticline with a NW-SE axial trace and SW vergence (Cooper, 2000). The NE-SW striking faults, interpreted as normal to strike slip (Friedmann and Stamp, 2006; McCutcheon, 2003), divide the Dome in several blocks (Cooper et al., 2003; Friedmann et al., 2004; Friedmann and Stamp, 2006). The stratigraphy includes the Pennsylvanian Tensleep Formation consisting of eolian sandstone deposits with interbeds of sabkha and shallow marine dolomites. The dataset used in this study is public (RMOTC, 2005a,b). It includes well data, well logs, formation micro imager (FMI) logs, and a 3D seismic cube across the anticline. For reservoir modeling of this structure, accurate fracture characterization is crucial. Numerous studies have focused on fracture characterization and modeling of reservoirs in the Wyoming area. Generally, fracture characterization is performed on different scales. Cooper (2000), Cooper et al. (2006), La Pointe et al. (2002), Schwartz (2006), and Gilbertson and Hurley (2006) agree on the existence of three dominant fracture sets that strike oblique, parallel and perpendicular to the fold axis. Several studies use fracture characterization and fracture modeling. Some studies use volumetric seismic attributes as guidance for fracture modeling (Smith, 2008; Wilson et al., 2013). Some authors employ seismic attributes in an unconventional approach: For example Ouenes et al. (2010) couple the seismic attributes with additional fracture drivers, in the so called continuous fracture modeling (CFM) technique. This approach assumes the identification of fracture drivers, their rating, validation and usage in order to build the fracture model. Thachaparambil (2015) use different seismic volume attributes in

order to extract seismic discontinuities from post-stack attributes into seismic discontinuity planes (SDP) containing the fracture properties such as orientation, length and shape.

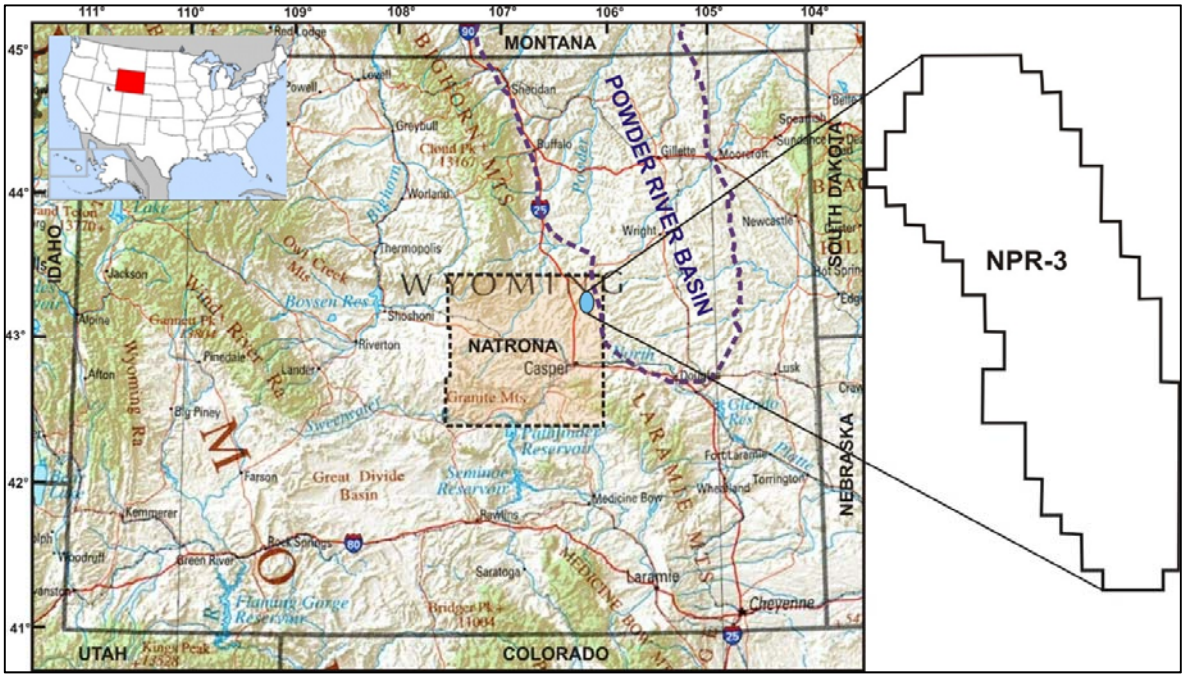

Figure 1. *Location of the Teapot Dome. Displayed are the general location of the Wyoming area (upper left map), the location of the Natrona County (light orange) and the Teapot Dome (blue) together with the Powder River Basin (dashed purple line). On the right side, a map view of NPR-3 is given (after Cooper, 2000). Modified from "The National atlas of the United States of America" U.S. Geological Survey, 2001.*

The main objective of this thesis is to develop and evaluate fracture models based on different approaches. Essentially the evaluation and uncertainty assessment of the techniques is performed on the resulting reservoir permeability. The approaches mainly differ in the guidance of the fracture intensity throughout the area. An additional objective is to perform a sensitivity analysis of the main fracture parameters in order to state their influence on the modeled results. In summary, the thesis focuses on the following topics:

1) Analysis of statistical laws used in fracture modeling;
2) Estimation of fracture parameters and sensitivity analysis;
3) Analysis of geostatic interpolation methods;
4) Application of seismic attributes as guidance in fracture modeling, and
5) Creation, evaluation and comparison of the fractured models.

The result of the thesis should provide a better understanding of the complexity and problems associated with modeling of NFR. In addition, the comparison of the models highlights the disadvantages of the standard modeling procedure, which delivers an inaccurate prediction of fracture intensity. Although the application of different seismic attributes delivers fracture permeability of similar range, the derived fracture models show differences in the direction and connectivity of high flow zones.

2. Geologic setting

The Rocky Mountain region is underlined by the numerous of uplifts and basins. They are formed in response to the horizontal shortening associated with two overlapping tectonic events, the Sevier and the Laramide orogenies (Gay, 1999). These events are expressed by different deformation styles. The deformations related to the Sevier orogeny are characterized by basement detached folding and thrusting (Stone, 1993; Gilbertson and Hurley, 2006).

On the other hand, the Laramide orogeny is characterized by fault propagation folds developed above the basement rooted faults. The Laramide orogeny took place from late Cretaceous to Paleocene. The NE-SW shortening formed the basement-cored uplifts striking normal to the direction of shortening (Dickinson and Snyder, 1978; Bird, 1998). The NW-SE trending basement cored uplifts are separated by sedimentary basins. In general, the axes of these basins are subparallel to the trend of the uplifts (Dickinson et al., 1988, Stone, 1993, Gao et al., 2011).

The Laramide basins comprises numerous anticlines, such as Elk basin anticline, Alcova anticline, Oil Mountain anticline, Flat Top anticline, that strike subparallel to the primary structures.

Figure 2a illustrates the main Laramide uplifts and basins of the Wyoming area. The Teapot Dome is a typical Laramide anticline trending sub parallel to the major structures of the area. It is an element of the larger Salt Creek complex, which contains several basement-cored anticlines (Doelger et al., 1993; Gay, 1999; Cooper, 2000; Chiaramonte, 2009), Figure 2b. The Teapot Dome is located near the southwestern edge of the Powder River basin and is surrounded by the adjacent uplifts (Sweetwater, Laramie, and Bighorn) and basins (Wind River, Bighorn, and Denver), Figure 2b.

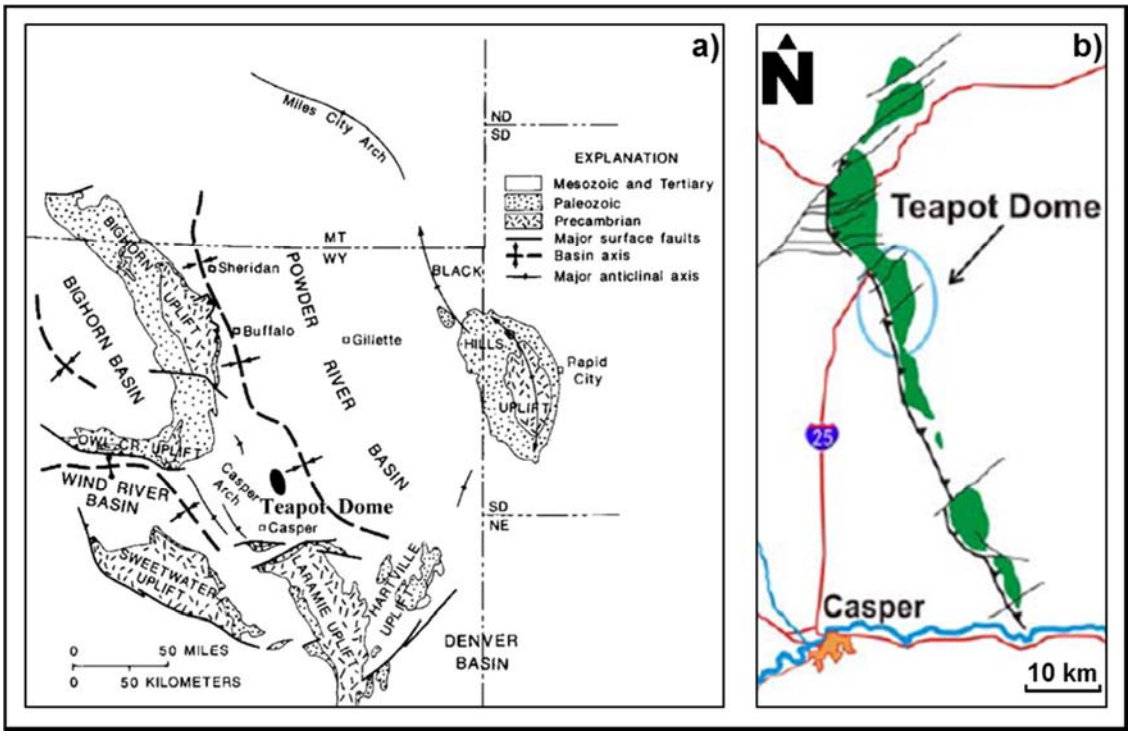

Figure 2. *a) Map of the Teapot Dome relative to the Laramide uplifts and basins in Wyoming (after Fox et al., 1991), and b) location of the Teapot Dome within the Salt Creek structural complex (green) (after Chiaramonte, 2009).*

2.1 Teapot Dome Anticline

The Teapot Dome is an elongated, asymmetrical, doubly plunging anticline above a high angle thrust fault with 35°-40° east-northeast dip (Cooper, 2000; McCutcheon, 2003; Chiaramonte, 2009). The Teapot Dome is characterized by shallow dips on the eastern flank and steeper dips on the western flank. This SW verging fold is underlined by a thrust fault that bounds the anticline on the west (McCutcheon, 2003, Milliken and Koepsell, 2003; Lorenz and Cooper, 2013). The sediments are folded over the thrust fault that offsets the basement and Paleozoic sediments and terminates within the Cretaceous sedimentary section above (Cooper, 2000; Lorenz and Cooper, 2013). The fold is more asymmetric near the basement while in the upper part (Cretaceous strata) the anticline is broader and less asymmetric with gentler limb dips (Lorenz and Cooper, 2013).

Along the eastern flank, structural elements are represented by normal to strike-slip faults striking approximately perpendicular to the fold hinge (Doll et al., 1995). The NE-SW striking normal to strike slip faults divide the dome in several blocks. In general,

these faults offset the basement and locally vary in orientation with very steep dip angles. These faults are noticeable on outcrops (Cooper, 2000) and seismic (McCutcheon, 2003). Figure 3 shows the structural map at the reservoir level. The main structures at Teapot Dome are the NW-SE striking anticline and NE striking normal to strike slip faults.

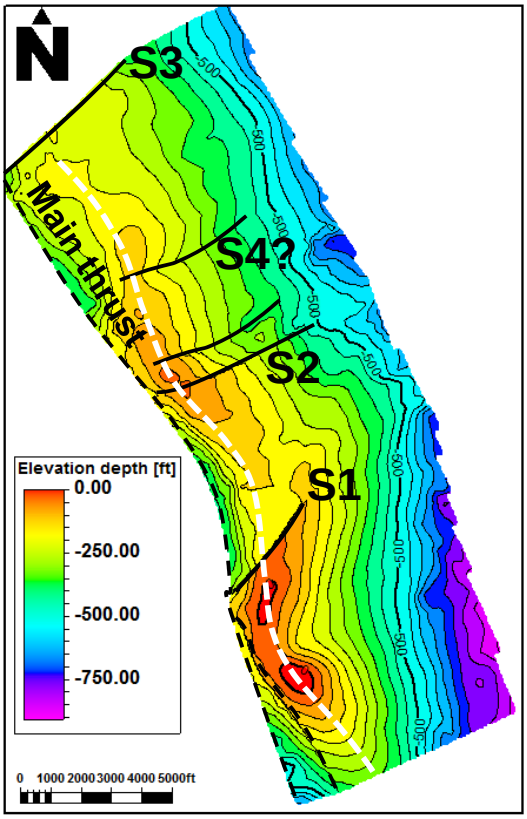

Figure 3. *The structure map of the reservoir top and main structures: solid lines S1-S4 represent the normal to strike slip faults; dashed black line marks the position of the thrust fault and white dashed line is the fold axis.*

McCutcheon (2003) interpreted and named these faults S1 to S4. The lateral offset at the surface and observed sub-horizontal striations suggest that they are tear or accommodation faults (Cooper et al., 2003; Friedmann et al., 2004; Friedmann and Stamp, 2006). The timing of these faults might be contemporary with the Laramide shortening (Friedmann and Stamp, 2006).

2.2 Stratigraphy

The typically hydrocarbon bearing reservoirs of Wyoming are tight fractured sandstone units. At Teapot Dome, the stratigraphic column comprises the Devonian to Cretaceous Formations. The Tensleep sandstone is one of the key producers of the Teapot Dome. In general this Formation shows changes in lithological units (i.e. from carbonates to clastic) due to different depositional environments during the Late Paleozoic (Zhang, 2007). The Tensleep sandstone overlies the Amsden Formation, which contains mostly dolomites. The upper bound is an unconformity, above which there is a regional seal corresponding to the Permian Goose Egg Formation of shales, carbonates and anhydrite (Li, 2014).

The Pennsylvanian sandstone sequence is 300 ft (100 m) thick and it is composed of eolian dunes intercalated with marine dolomitic deposits (Zhang, 2007). The intercalations of dolomites vary through the Tensleep section. Also, the depositional environment changes from dominantly marine (bottom) with thin sandstones and thicker carbonates, to non-marine on the top with cross bedded sandstones and thin carbonates (Zhang, 2007; Li, 2014). The presence of the thin dolomite layers within the inter-dune deposits can be explained by periods of transgression. This is further followed by exposure that leads to an unconformity on the top of the unit (Friedmann and Stamp, 2006). The Tensleep Formation is divided into the lithofacies: eolian dunes, interdunes and sand sheet based on the sandstone dolomite ratio (Zhang, 2007). The sandstones A and B are the most important ones within the Formation, Figure 4. In general, the sandstone units are permeable zones but their properties depend on the degree of cementation, which in turn reduces the effective porosity and permeability. The average porosity is 8% while the average permeability is 80md (Friedmann and Stamp, 2006; Chiaramonte, 2009). The main producing part of the Formation is the B sand (Figure 4), which contains the highest degree of continuity of sandstone bodies. The thickness of the B sand is approximately 100 ft (Friedmann and Stamp, 2006).

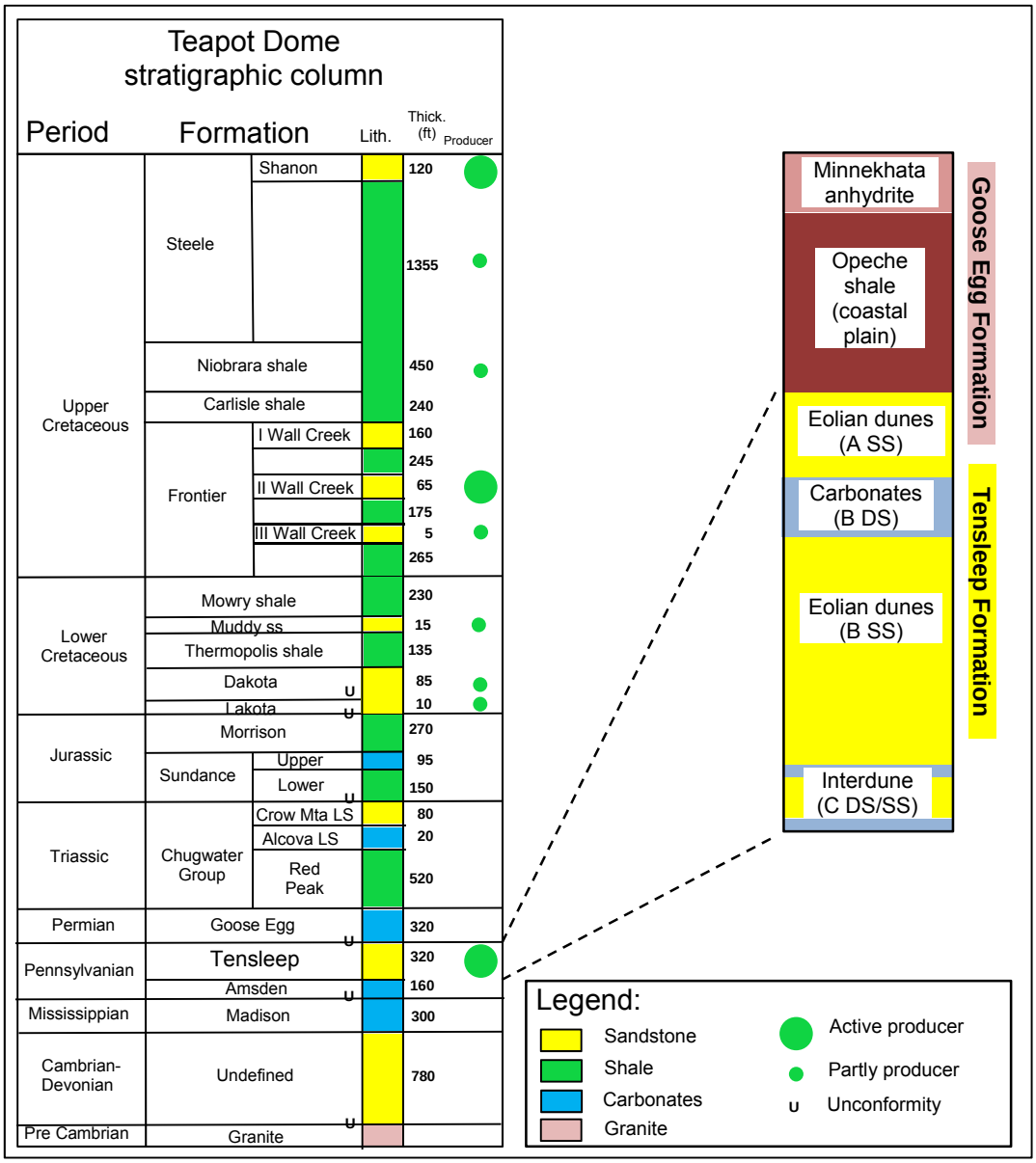

Figure 4. *Stratigraphic column of the Teapot Dome (left- courtesy of RMOTC), and lithological units within the Tensleep formation (right- after Chiaramonte, 2009).*

2.3 Fractures at Teapot Dome

Numerous studies analyzed the fractures at Teapot Dome and adjacent areas (Cooper, 2000; Cooper et al., 2006; Schwartz, 2006; Gilbertson 2006; Lorenz and Cooper 2013). These studies are based on outcrop observations and interpretation of the core data and FMI logs. These interpretations document the changes in fracture patterns with depth (Lorenz and Cooper, 2013). Cooper (2000) performed a fracture characterization based on outcrops of the Cretaceous Mesaverde Formation. His

analysis reveals three main sets of fractures showing different orientations relative to the fold hinge. These fracture sets are oblique, parallel and perpendicular to the fold hinge. The all sets comprises the extension fractures that are vertical or bed normal in case of folded layers. They are formed with all three principal stresses in compression and opened against the minimum stress (Lorenz and Cooper, 2013). The hinge oblique set is documented through all the region with similar orientation and suggests that it may have been formed prior to the folding (Garrett and Lorenz, 1990; Hennings et al., 1998; Cooper, 2000; Lorenz and Cooper, 2013). The fracture sets parallel and perpendicular to the hinge consist of bed normal extension and high angle conjugate shear fractures. These two different types of fractures strike subparallel, Figure 5. The hinge parallel and perpendicular sets are formed in response to the bidirectional extension normal and parallel to the fold hinge (Cooper 2000, Lorenz and Cooper 2013). The timing of these two sets is closely linked to the folding. Based on his analysis, Cooper (2000) proposes a 3D conceptual fracture model for Teapot Dome as illustrated in Figure 5.

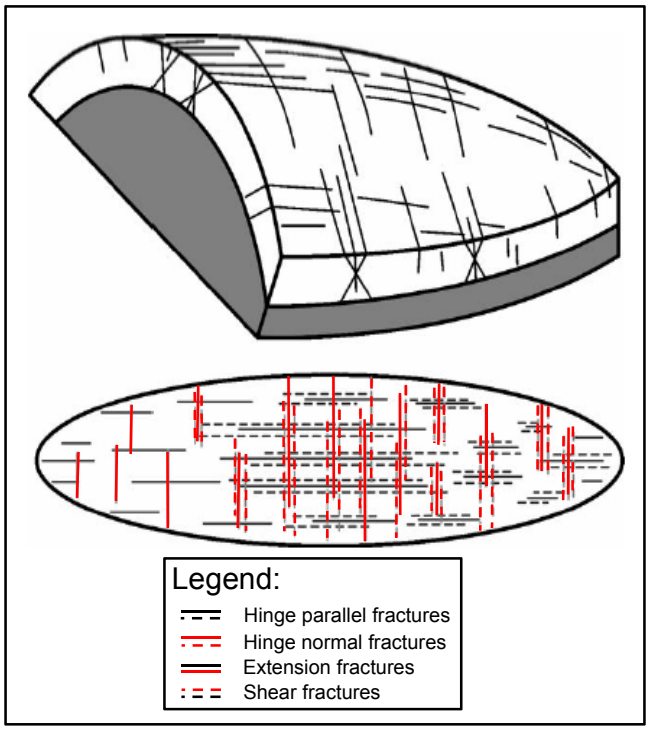

Figure 5. *Conceptual 3D model (above) and plan view (below) of fractures pattern within the Teapot Dome (after Cooper, 2000). The model is based on fracture observations from outcrops of the Mesaverde Formation.*

This conceptual model differs from the model proposed by Stearns and Friedman (1972) for thin-skinned basement cored thrusts. The main difference refers to the orientation of the conjugate pair of shear fractures. Whereas Stearns and Friedman (1972) model documents shear fractures obliquely transecting the fold hinge, Cooper (2000) model considers the shear fractures striking parallel and normal to the hinge. The distinct folding mechanisms and the depth of the thrust relative to the analyzed fractured layers explain these differences.

The interpretation of FMI logs and cores provides insight into the fracture patterns within the Tensleep Formation. Contrary to the interpretation of the Mesaverde Formation where the dominant sets of fracture are normal and parallel to the hinge, the dominant fracture set within Tensleep strata strikes oblique to the fold hinge, Figure 6. The dominant oblique set involves extension fractures and high angle shear fractures that are striking sub-parallel to parallel. These two types of fractures reveal the maximum horizontal stress prior to the fracturing. According to Lorenz and Cooper (2013), the fractures of the Tensleep formation record the NNE-SSW extension initiated by horizontal shortening oblique to the fold hinge in WNW-ESE direction.

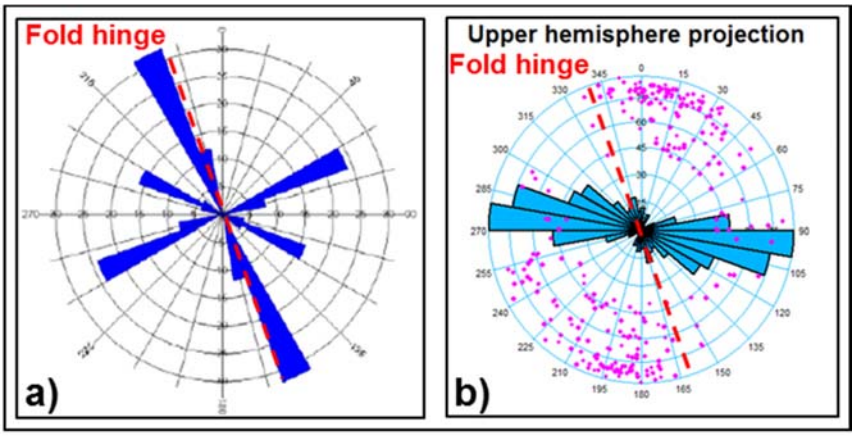

Figure 6. *The dominant fracture sets of the Teapot Dome at different stratigraphic layers: a) Mesaverde formation (after Cooper, 2000) and b) at Tensleep formation.*

The present day stress can be inferred from drilling induced fractures. The orientation of these fractures from FMI logs suggests that the present maximum compression stress strikes oblique to the fold hinge and parallel to the horizontal maximum stress responsible for the creation of the dominant fracture set (Schwartz, 2006; Lorenz and Cooper, 2013). Also, Lorenz and Cooper (2013) suggest that orientations of the dominant set, paleo and present day maximum horizontal stresses record the stress

orientation responsible for the thrusting. The differences between the dominant fracture sets within the two Formations can be explained by the degree of folding through the sediments. Shallower layers are more folded compared to the deeper layers. Consequently, the fractures in the Tensleep Formation are mostly formed in response to the extension normal to the horizontal shortening in the NW- SE direction. On the other hand, the fractures in the more folded Cretaceous layers are formed in response to extension parallel and normal to the fold hinge (Lorenz and Cooper, 2013). The sets parallel and normal to the hinge are also present in Tensleep Formation but in considerable less extent.

3. Dataset

The Rocky Mountain Oilfield Testing Centre (RMOTC) acquired the dataset used in the project. It consists of four 2D seismic lines, a 3D seismic cube and four wells penetrating the Tensleep Formation. The dataset is public (Friedmann and Stamp, 2006; RMOTC, 2005a, 2005b).

The 2D seismic includes 4 lines of different length in the SW-NE direction (Figure 7). The length of the lines B and C is 5,5 km, line D is 4 km and line E is 7,5 km (Figure 7). In addition, one cross-line along the anticline (line A) has a length of approximately 13 km (Figure 7). The maximum two-way travel time of the vintage is 4000 ms. The 3D seismic data, consist of 345 in-lines and 188 cross-lines with a bin size of 110 ft (33 m). The total coverage of the cube is approximately 70 km^2. The maximum two way-travel time is 3000 ms. The 3D seismic shows generally good quality. An exception is the western part of the survey, in front of the anticline forelimb where the data is characterized by chaotic pattern in reflectors. Also close to the edges of the survey, random noise affects the quality of the reflectors. A post-stack seismic time EXCEL Geophysical Services Company in Denver, Colorado (RMOTC, 2005a; Li, 2014) interpreted migrated volume. This interpretation provides the picked horizons for the stratigraphic units within the Teapot Dome: the Second Wall Creek Formation (KF2), the Dakota Formation, the Tensleep Formation, the Tensleep base and the basement (McCutcheon, 2003). The data also include time-to-depth relationships and synthetic seismograms (Li, 2014). Figure 7 displays a map with the location of the 2D lines and the 3D seismic survey together with an in-line section in the time domain.

In addition, the dataset contains four wells which penetrate the Tensleep Formation. All four wells (i.e. 25-1-X-14, 48-X-28, 67-1-X-10, 71-1-X-14) are located along the fold hinge and penetrate the Tensleep reservoir. All wells include FMI logs, lithology logs, fracture measurement logs and well tops. Also the interpretation of FMI logs is a part of the comprehensive dataset. Figure 8 illustrates a map with the position of the wells together with rose polar diagrams showing the fracture strikes. Also shown is a well with wireline logs and fracture data within the Tensleep interval and a stereonet with the provided fracture point data.

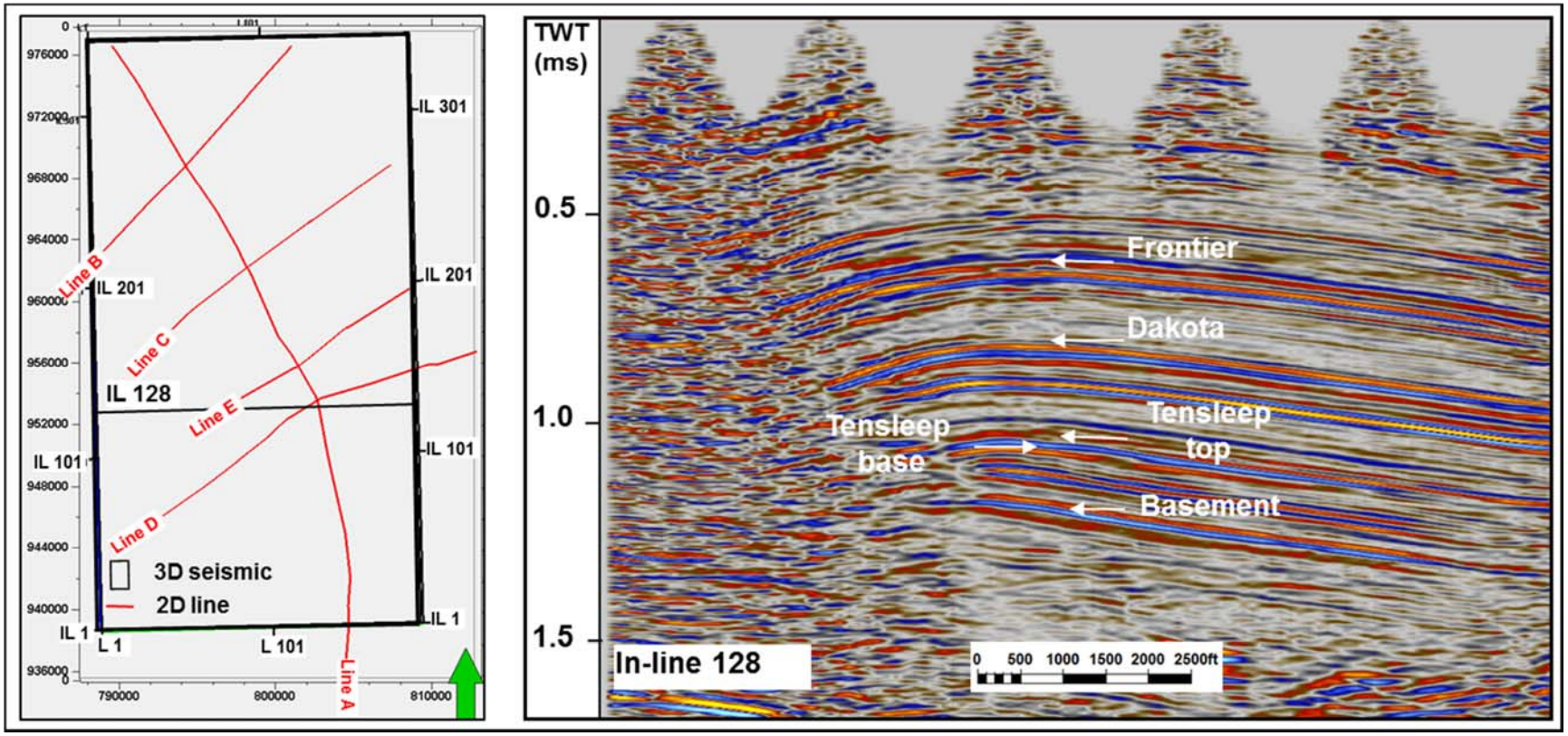

Figure 7. *The seismic dataset. Navigation of the 2D lines and the seismic 3D cube (left), and example of a seismic 3D line (in-line 128) with interpretation of the main horizons (right).*

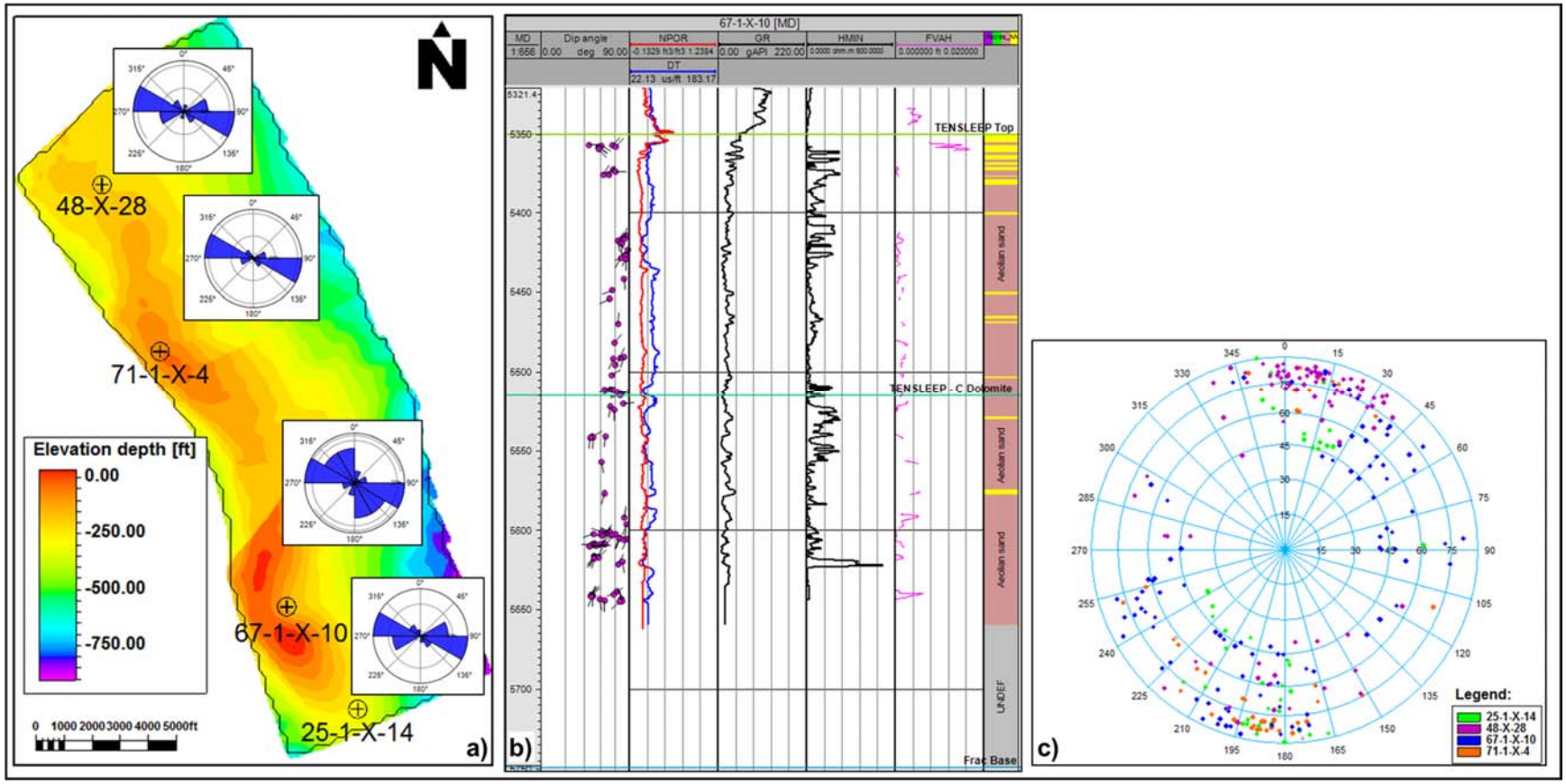

Figure 8. *The well data. a) The structure map of the Tensleep top with location of the wells and polar rose diagrams displaying the strike of the fractures, b) Example of one characteristic well (67-1-X-10) showing the provided logs (from left to right): fracture point data, neutron and density logs, gamma ray log, resistivity log, and electric fracture aperture log; c) Fracture point data displayed on upper hemisphere projection for all wells.*

4. Methodology

The methodology involves two different approaches in fracture modeling: the standard method and the method guided by seismic attributes. The difference between these two methods lies in the way fracture intensity is modeled. Fracture intensity is an important fracture attribute because it guides the fracture simulation. It is estimated from the fracture point data derived from the well data and upscaled into the 3D model. Typically, the standard method employs Kriging or Sequential Gaussian Simulation (SGS) to interpolate the fracture intensity of the 3D grid. This method can deliver highly inaccurate results in case of limited well control. The second approach tries to reduce this uncertainty, through controlling the fracture intensity interpolation via seismic attributes. For both methods, the fracture parameters fracture length, aperture, and permeability need to be provided. The estimation of these parameters is based on statistical laws derived from analogue data. The derived fracture properties serve as input together with the modeled fracture intensity for the generation of a Discrete Fracture Network (DFN). Finally, the models derived from the two different methods are compared by evaluating the upscaled fracture permeability, which is derived from the aperture and intensity of the simulated fractures. The methodology scheme shown in Figure 9 summarizes the workflow used in this thesis and displays the steps for each of the two approaches.

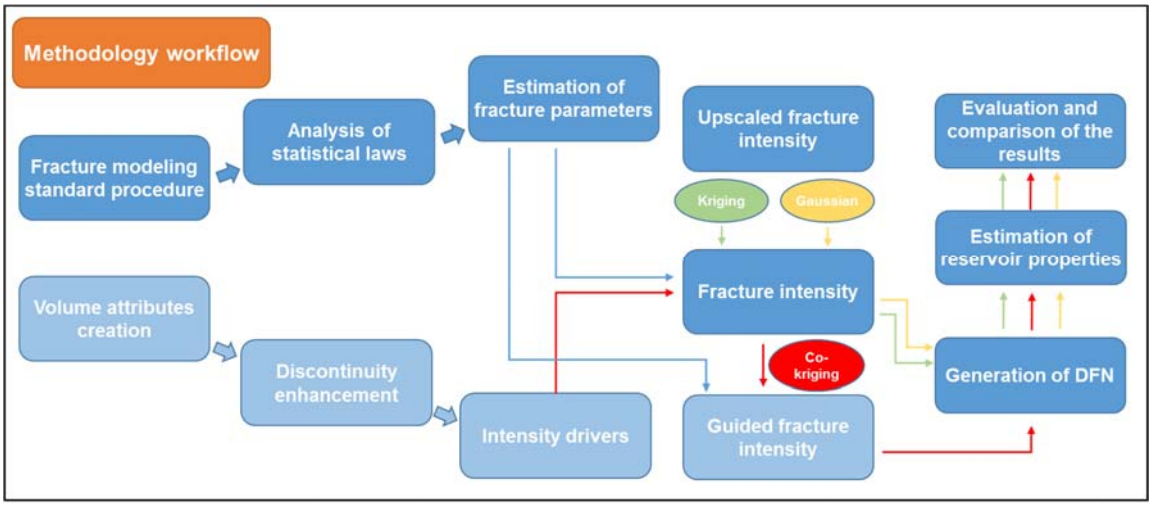

Figure 9. *Workflows for fracture modeling based on the standard approach (dark blue) and on seismic attributes (light blue).*

4.1 Basic workflow for fracture modeling

The initial modeling step is the quality control of the logs used for fracture measurements. In general, the formation micro-imager (FMI) log delivers the fracture point data that reveals essential information of the fracture parameters dip, azimuth and aperture. One of the most essential parameter for the modeling is the fracture intensity. The fracture intensity can be derived in several different ways. The selected method depends upon the dimension that is selected for determining fracture intensity. Table 1 shows the measurements of fracture intensity in the 1, 2 and 3D.

Table 1. *Different values of the fracture intensity (after Dershowitz and Herda, 1992).*

	Dimension of fracture			
Dimension	**Number**	**Length**	**Area**	**Volume**
1D	P10	P11		
2D	P20	P21	P22	
3D	P30	P31	P32	P33

Generally the intensity refers to the fracture spacing (Sf) that is dependent on the fracture orientation and can only be used under the assumption of sub-parallel fractures (Dershowitz and Herda, 1992). The intensity measured in the 1D represents the number of fractures per unit length and is named as $P_{10.}$ This value is inversely proportional to the fracture spacing (Dershowitz and Herda, 1992). The intensity measured in the 2D space is expressed either as the number of fractures per unit area (P_{20}) or as the length of the fracture traces per unit area (P_{21}).

In general, the intensity defined in 1D and 2D is dependent on the orientation and shape of the fractures as well as on the orientation and shape of the measurement region (Lee et al., 2011). Consequently, these intensity measurements cannot be used in 3D fracture modeling. Figure 10 shows the fracture intensity estimation for the 1D and 2D.

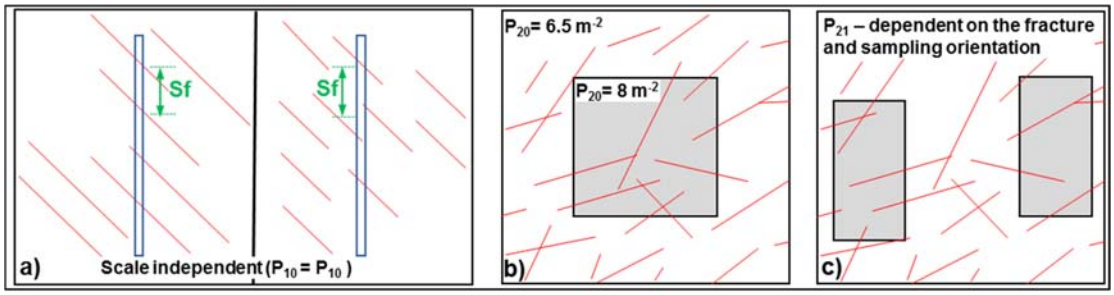

Figure 10. *Fracture intensity represented in 1D and 2D: a) Intensity in 1D - P_{10}, dependent on orientation; b) intensity in 2D – P_{20} dependent on fracture size and c) intensity in 2D – P_{21} dependent on the fracture and sampling area orientation (after Dershowitz and Herda, 1992).*

The 3D modeling requires fracture intensity defined in a 3D region, which is independent of the fracture size and orientation. The intensity P_{32} represents the fracture area within a reference volume. Direct observation of the intensity based on P_{32} is practically impossible. However, a relation between the intensity values P_{32} and P_{10} can be derived and is given by Equation 1 (Dershowitz and Herda, 1992; Lee et al., 2011):

$$P32 = C10 * P10 \qquad \text{Equation.1}$$

where C10 is a constant dependent upon the orientation of the fractures and the borehole.

The intensity conversion is essential for large volumes, for instance outcrops, where the fracture orientation plays an important role, figure 10c. For very small volumes such as boreholes, the P_{32} intensity can be related to the number of the fractures per unit length (P_{10}). The diameter of the borehole is significantly smaller than the fracture length, which means that each fracture can be represented by a fracture point independent of the angle at which the fracture intersects the borehole. In fracture modeling, the intensity is derived from the slope of the cumulative distribution of the fracture point data.

In addition, the correct borehole orientation plays an important role in estimating the fracture intensity. Prior to the value estimation, the angle between fractures and borehole needs to be considered. The procedure is well known as a correction of the borehole deviation (Baytok, 2010; Schlumberger, 2013). For instance, vertical boreholes have a smaller probability to sample vertical fractures compared to horizontal wells, Figure 11. Therefore, the borehole path needs to be corrected in order to estimate the fracture intensity more accurately.

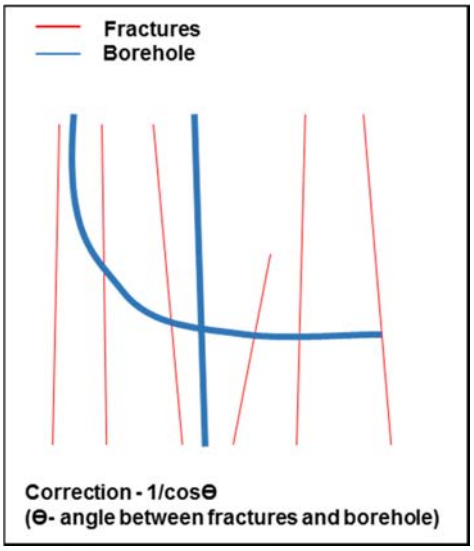

Figure 11. *Correction for borehole deviation. The horizontal well will result in higher intensity value.*

Once the intensity data has been derived, it needs to be sampled into a 3D grid and interpolated in order to get a 3D property. The most common interpolation algorithms used for modeling are Kriging and Sequential Gaussian Simulation (SGS).

In addition, fracture modeling requires an estimation of the fracture parameters. From the fracture point data, the fracture orientation can be inferred in form of the dip angle and azimuth. In addition, electrical logs allows estimating the fracture aperture. The fracture length cannot be inferred from the logs since the borehole data are usually affected by sampling artifacts. These sampling artifacts are known as truncation and censoring. The truncation effect is caused by the low sampling resolution and leads to the underestimation of the small fractures (Ortega Pérez, 2002). In addition, due to the limited size of the sampling domain, the larger fractures usually extend further than the sampling region. This leads to poor sampling of the large fractures that can result in their underestimation. The impact of the censoring usually is associated with measurements of fracture length. Thus, fracture length estimation requires a combined usage of data from different scales in order to capture the parameter distribution. For instance, the data collected along the outcrops delivers insight into the length distribution. The gathered data indicate that the fracture length and fracture aperture are functions of the cumulative frequency of the fracture, which in turn is a direct measurement of fracture intensity (Ortega et al., 2006). Statistical laws describe the measured relationship between fracture parameters length and aperture with fracture

intensity. These laws are used to assign stochastically the fracture parameters to the simulated fractures of the model.
After the generation of the fracture network model, the fracture properties are upscaled into the model in order to estimate the reservoir permeability.

4.1.1 The analysis of the statistical laws

In general, the fracture modeling and the generation of the discrete fracture network (DFN) use a number of statistical tools to model fracture length and aperture. These distribution laws describe the observed fracture length and aperture as a function of fracture intensity. Typically, distributions used in fracture modeling are normal, log normal, exponential and the power law. In Table 2, the statistical laws are describe together with their main controlling parameters.

Table 2. *Statistical laws utilize in fracture modeling*

Statistical law (distribution)	Equation	Controlling parameters
Normal	$p(x) = \frac{1}{\sigma\sqrt{2\pi}}\, e^{-\frac{(x-\mu)^2}{2\sigma^2}}$	μ - mean σ- st. deviation
Log-normal	$p(x) = \frac{1}{x\sqrt{2\pi\sigma^2}}\, e^{-\frac{(\ln x-\mu)^2}{\sqrt{2\sigma^2}}}$	μ - log mean σ- st. deviation
Exponential	$p(x) = \frac{1}{\beta}\, e^{-\frac{x}{\beta}}$	β - scale parameter
Power law	$p(x) = \frac{\alpha-1}{X_{min}}(\frac{X}{X_{min}})^{-\alpha}$	α – exponent Xmin- distribution lower bound

Changing these parameters affect the fracture distribution allowing to reproduce, for instance, the distribution of measured fractures properties. As an example, Figure 12 shows the fracture length for a normal distribution and different mean values.

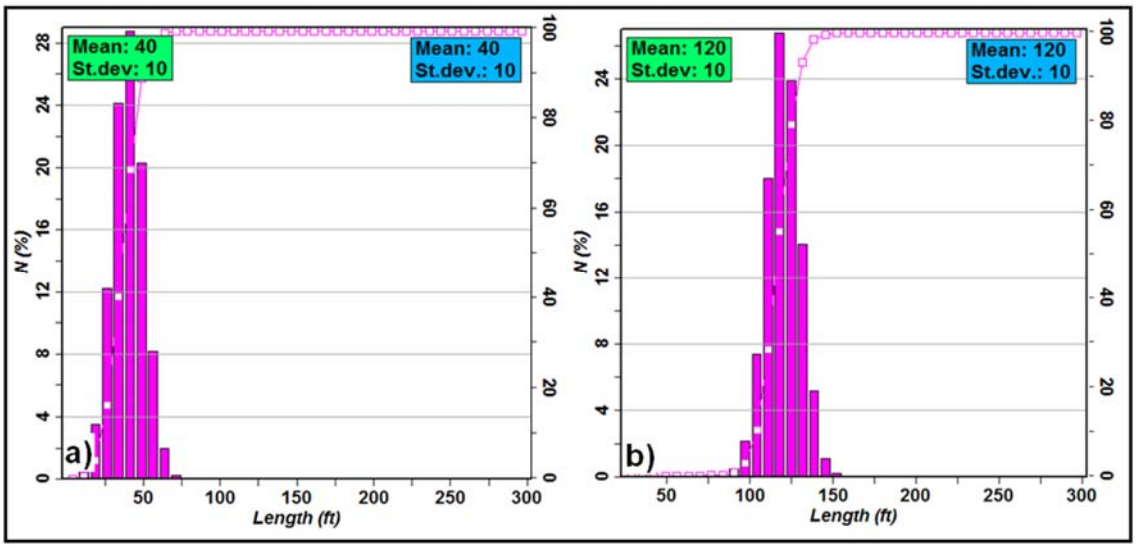

Figure 12. *Example of normal fracture length distribution presented by histogram and cumulative distribution function (CDF-pink line). Green boxes display input parameters and blue boxes display the statistics of the modeled fracture parameters.*

4.1.2 Estimation of fracture parameters

The fracture modeling requires an assessment of the geometrical parameters such as fracture length, orientation and aperture. Fracture logs provide information about the fracture dip angle and azimuth. These parameters are integrated into the model in form of the mean dip and azimuth. Three different algorithm proposed by Fisher, Bingham and Kent (Schlumberger, 2013) are provided by Petrel which allow to introduce a user-controlled uncertainty for the orientation of the simulated fractures around the provided mean value in a controlled way. Figure 13 shows an example of simulated fracture orientations based on the three algorithms and the impact of their parameters on the distribution.

In general, the Fisher method is similar to the Normal distribution and requires the mean orientation and a so-called concentration parameter as input. The Kent orientation introduces an anisotropy factor, which results in a more elongated distribution of the fracture orientations compared to the Fisher distribution. The Bingham distribution is defined by a mean orientation and two concentration parameters, azimuthal (Ac that controls the variations around mean azimuth) and radial concentration (Rc that controls variation around mean dip).

Fracture length cannot be derived from well logs. Therefore, the estimation technique employs the data from analogues. Numerous studies performed a fracture

characterization based on outcrops (Cooper 2000; Cooper et al., 2006; La Pointe et al., 2002; Gilbertson and Hurley 2006; Wilson et al., 2015). The resultant statistical laws can be used to assign a fracture length to the simulated fractures.

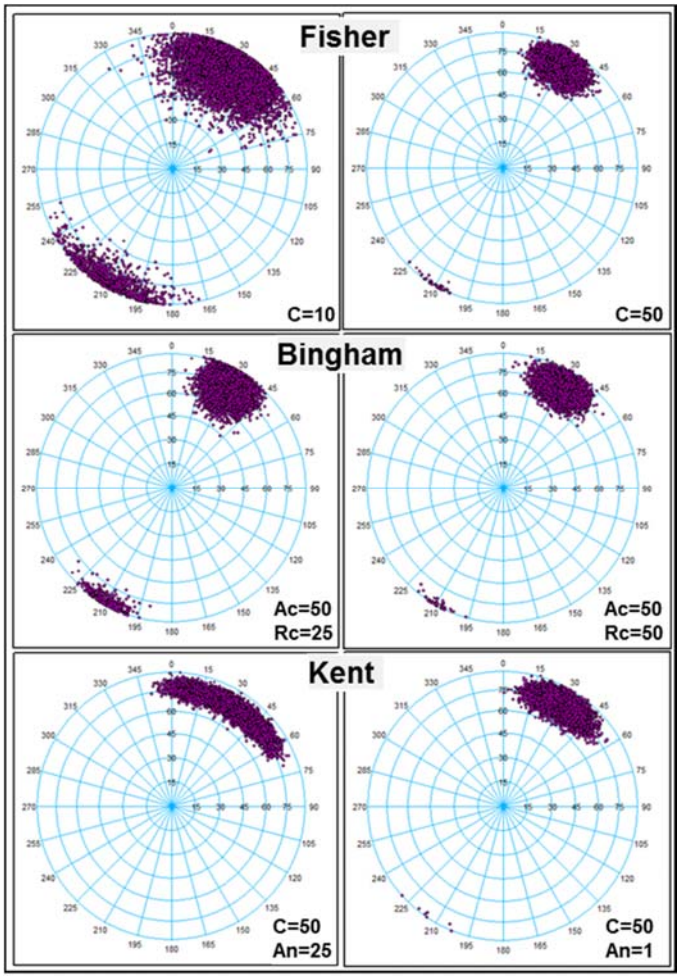

Figure 13. *Three distributions of fracture orientation: Fisher distribution (upper), Bingham distribution (middle) and Kent distribution (lower). In all three distributions, the concentration parameters control the variation around the mean orientation values.*

The fracture aperture needs to be assigned to the simulated fractures in a similar way like the fracture length. Fracture apertures can be inferred from FMI logs. However, in case of limited data, the measurements can be highly uncertain. In order to estimate the aperture distribution more reliably the measured distribution can be combined with statistical laws. This can be done by adjusting the parameters of the selected statistical law in order to match the measured distribution of the fracture aperture.

Numerous studies refer to the relation between fracture length and aperture (Cowie and Scholz, 1992; Olson, 2003; Scholz, 2002; Vermilye and Scholz, 1995). The fracture aperture can be modeled in two ways: independently and related to the fracture length. Instead of the random assignment of the aperture to the fractures following the selected statistical law, a better approach is to take the relationship between aperture and length into account in fracture modeling. The studies mentioned above analyze the different fracture modes. Based on the displacement character (opening or shearing) the fractures are classified into three modes noted as opening (mode I), sliding (mode II) and tearing (mode III) mode fractures (Fossen, 2010; Klimczak et al., 2010). Mode I fractures are characterized by a displacement perpendicular to the fracture walls while modes II and III involve shear displacement perpendicular or parallel to the fracture edge, respectively (Fossen, 2010). The Figure 14 shows the three fracture modes.

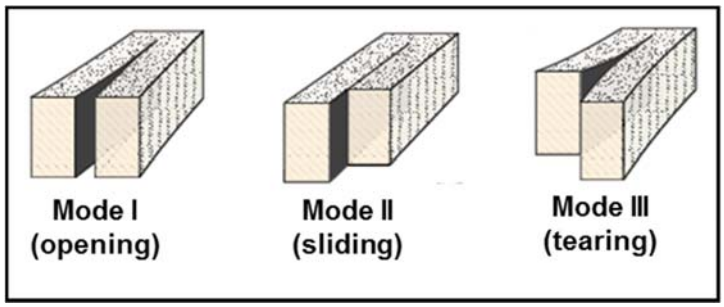

Figure 14. *Three different fracture modes (Fossen, 2010).*

There are different ways to define the aperture to length relation. For instance, Vermilye and Scholz (1995) propose a linear relationship between the aperture (D_{max}) and the fracture length (L) based on studies performed on sliding and tearing mode discontinuities (mode 2 and 3):

$$D_{max}=\gamma L \qquad \text{Equation (2)}$$

where γ represents a constant. In addition, Olson (2003) analyses the opening mode fractures (mode 1) and suggests the square root relation:

$$D_{max}=\alpha L^{0,5} \qquad \text{Equation (3)}$$

where α is a proportionality coefficient that is a function of the fracture toughness, Poison`s ratio and Young`s modulus (Klimczak et al., 2010). In this study, the fracture modeling uses the square root aperture to length relation (Equation 3).

The fracture permeability can be either, modeled independently or linked to the fracture aperture. The permeability is linked to the fracture aperture by the adaptation of the cubic law, under the assumption that fractures can be described by two parallel planar planes and that the flow within the fractures is laminar (Snow, 1969; Witherspoon et al., 1980), Equation 4:

$$K = \rho g\ (12\mu)^{-1} b^2 \qquad \text{Equation (4)}$$

with: K – hydraulic conductivity for the diagonal tensor components (in x, y z directions); b - aperture or width between the fracture walls; ρ - fluid density; g - the gravitational acceleration; μ - fluid viscosity.

Since the assessment of the fracture parameters shows a high level of uncertainty, a sensitivity analysis is important. This can be done by defining three sets of parameters representing the low, base and high case. Fracture models are calculated that keep all parameters to the base case with the exception of one. The models are compared through upscaling the fracture permeability and comparing their distributions, for instance in form of a Tornado diagram. The performed analysis allows identifying those parameters that are most influential on the reservoir parameters

4.1.3 Generation of the fracture intensity by the interpolation algorithms

The estimation of the intensity at the wells is described in section 4.1. The derived fracture intensity needs to be modeled. The two methods, Kriging and Sequential Gaussian Simulation (SGS) are the most commonly used algorithm for interpolation. The Kriging algorithm delivers an optimal interpolation in the sense of a best linear unbiased estimate at any location (Bohling, 2005). On the other hand, SGS delivers numerous realizations based on the same set of variables. Both algorithms are based on the variogram model derived from the input data. Also they honor the mean and variance of the input data. In addition, SGS provides a model data distribution similar to the input data.

The variogram model refers to the spatial variation of the data (Ringrose and Bentley, 2015). In general the variogram delivers the mean variance of data pairs of similar distance. Graphically, it is represented by the mean semi-variance as a function of the separation distance, Figure 15. The approximation of the semi-variance by an

analytical function delivers the variogram model. This model delivers the main variogram parameters sill, nugget and anisotropy range that are used in Kriging and Gauss simulation. Figure 15 shows an example of a sample variogram with the model (red line) and the definition of the main parameters. Among all parameters the variogram range is the crucial. It reveals the distance (range) at which the data do not show the spatial relationship. Consequently, a large range means a more homogeneous data distribution (Ringrose and Bentley, 2015). Also, in case of anisotropy of the data the spatial relationship varies with different directions (Bohling, 2005).

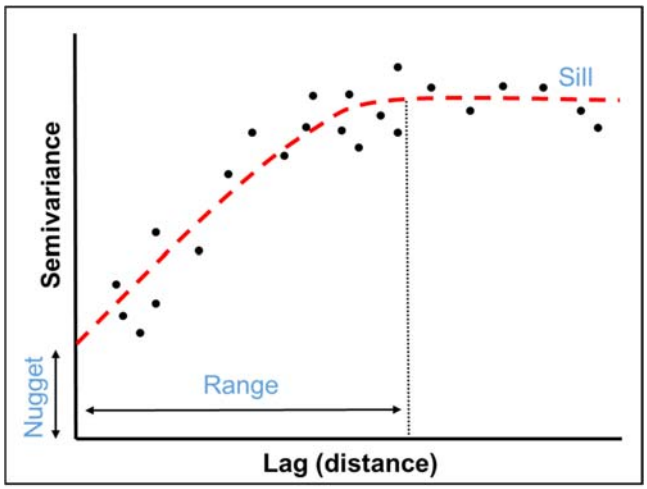

Figure 15. *An example of semi variogram model with its essential parameters (after Ringrose and Bentley, 2015).*

The variogram modeling is achievable only in case of a sufficient amount of data. Due to the limited data of this study, the sample variogram is too noisy to allow a reliable modeling. Consequently, three sets of the variogram parameters are defined in order to study the behavior of both interpolation algorithms. Figure 16 shows examples for the Kriging and SGS based on different horizontal variogram ranges. It can be observed that the variogram range controls the radius of influence of the input data. In case of SGS, it also controls the size of the patches of high and low intensity. In addition, Figure 17 shows two models based on SGS with identical parameters but different seeds. The two simulations honor the same basic statistics of the input data: same mean, variance and histogram; however, they show a different distribution of the intensity.

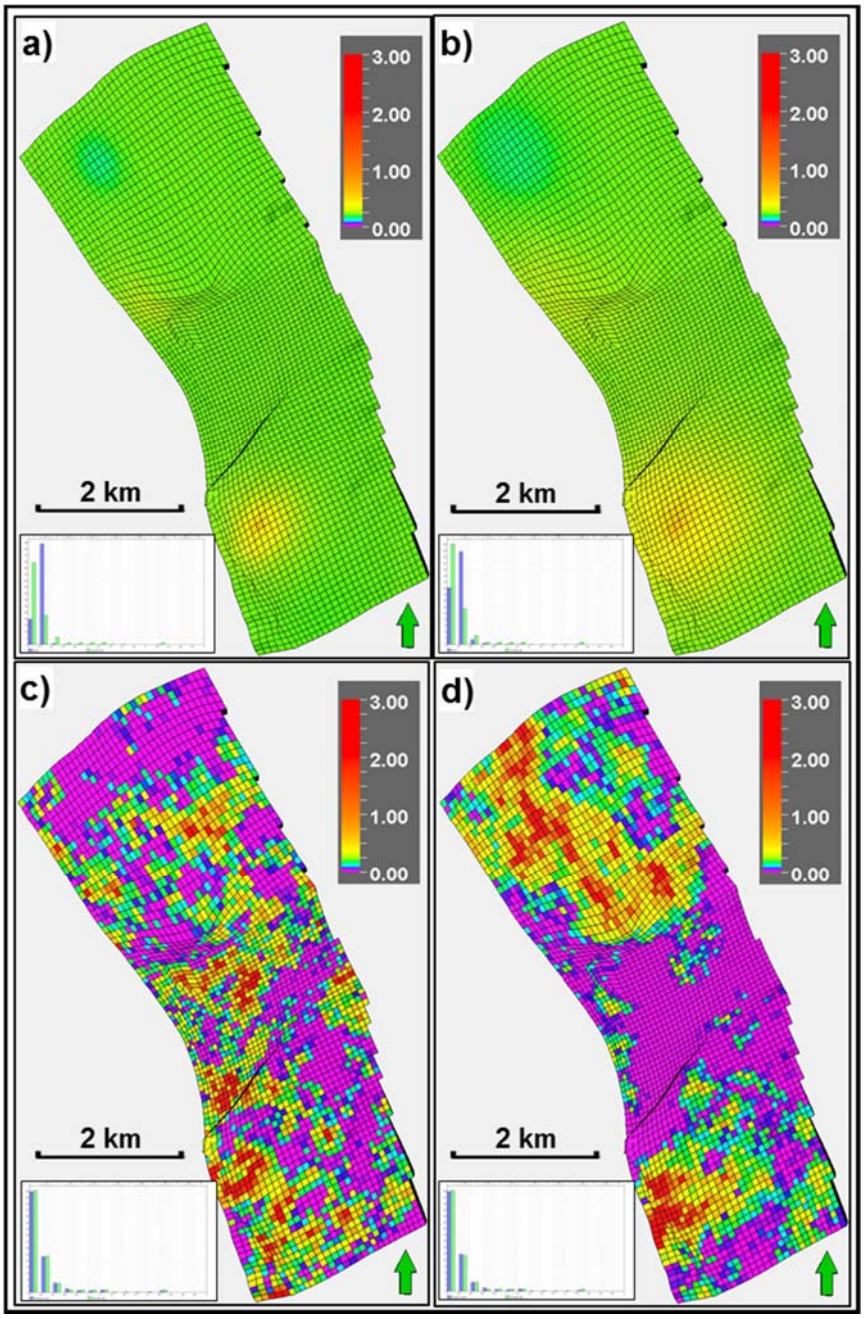

Figure 16. *An example showing the influence of the different variogram ranges on the intensity: Kriging algorithm a) small variogram ranges, b) large variogram ranges, and SGS c) small variogram ranges and d) large variogram ranges.*

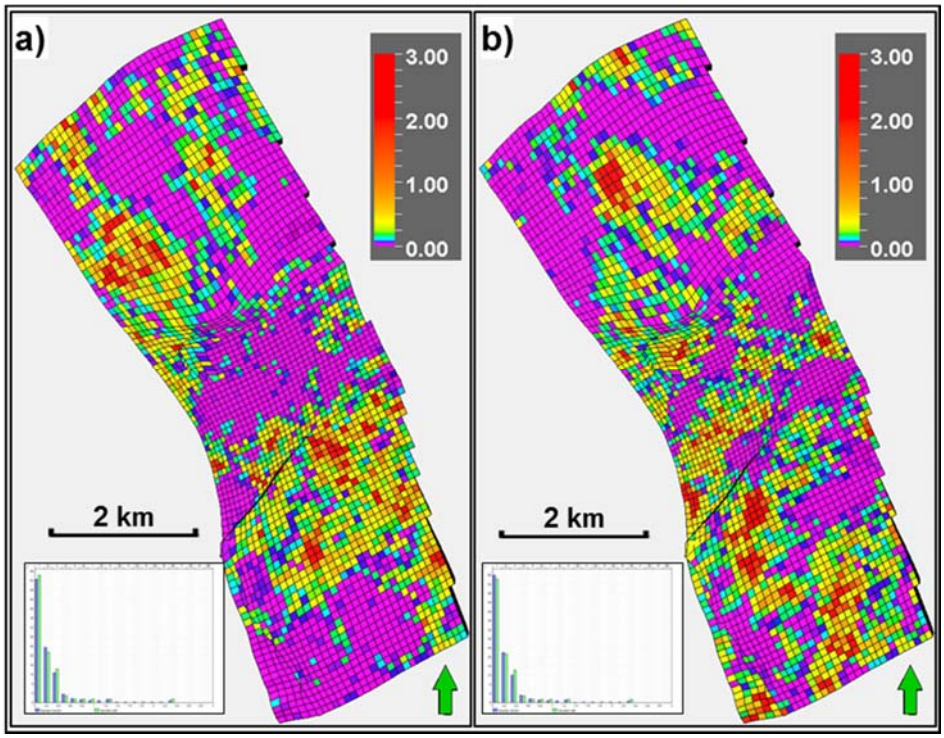

Figure 17. *Fracture intensity based on SGS and the parameters of figure 16: a) Seed 25000 and b) Seed 12000.*

4.2 Application of seismic attributes in fracture modeling

The detection of fracture swarms and small scale faults can be difficult, since they are below seismic resolution (Marfurt and Chopra, 2006). In addition, individual fractures cannot be detected by seismic. However, fractures are generally related to the distorted seismic reflectors and are observed in the vicinity of faults. During the last decades seismic attributes have been developed that are well suited for a detailed structural analysis allowing to identify fracture swarms and subtle faults (Anees, 2013; Lefranc et al., 2012). In general, their successful usage is closely linked to advances in acquisition and processing techniques of seismic. The attributes are applied either on interpreted seismic horizons or on seismic volumes. Numerous studies refer to surface attribute fracture prediction (Hart et al., 2002; Roberts, 2001). However, the reliable application of surface attributes strongly depends on accurate horizon interpretation that consequently entails additional uncertainties (Marfurt and Chopra, 2006). On the other hand, volumetric seismic attributes are independent of seismic horizon interpretation and are powerful tools to delineate the faults and small scale

discontinuities. Once the seismic attributes that show the fault and fracture swarm pattern convincingly are identified they need to be converted into fracture intensity.
The usage of seismic attributes in fracture modeling requires a systematic approach that involves the following steps:
1) attribute derivation and analysis;
2) additional discontinuity enhancement thru conditioning the attribute cube;
3) attribute sampling into the 3D grid and
4) fracture intensity modeling using co-kriging method guided by seismic attribute.
The following sections describe the methodology in more detail.

4.2.1 Creation of the multiple volume attributes

The usage of attributes for structural delineation is well documented by many researches (Aqrawi et al., 2012; Klein et al., 2008; Marfurt and Chopra, 2006). The ability of the fault identification by seismic attributes highly depends on the seismic resolution and the seismic response of the target zone (Thachaparambil, 2015). Structural smoothing allows improving the signal to noise ratio and enhancing the continuity of seismic reflectors. The used algorithm is a Gaussian filter that is guided by the dip and azimuth of the local structures (Randen et al., 2003). In addition some attributes (e.g. amplitude contrast) allow directional filtering that highlights the features in a particular direction (Aqrawi et al., 2012).
Especially suitable seismic attributes for structural interpretation are the so-called geometric attributes. This group of attributes is based on a multi traces analysis and includes chaos, curvature, amplitude contrast, consistent dip, edge detection and variance. The chaos attribute investigates the chaotic signal (Baytok, 2010) while the variance measured variations in the signal, delivering a larger variance in faulted areas (Randen et al., 2001). In addition, the curvature attribute is related to broken seismic reflectors, recording the curvature of the amplitude field (Klein et al., 2008). The amplitude contrast displays the negative and positive amplitudes that correspond to the areas without and with discontinuities, respectively. In general, many attributes require an adjustment of their parameters in order to optimize the visualization of the fault pattern. The methodology uses the multi-trace attributes discussed above which are also used in published studies for fault pattern recognition (Thachaparambil, 2015;

Wilson et al., 2015). The selected attributes are displayed in Figure 18 for a time slice within the time range of investigation.

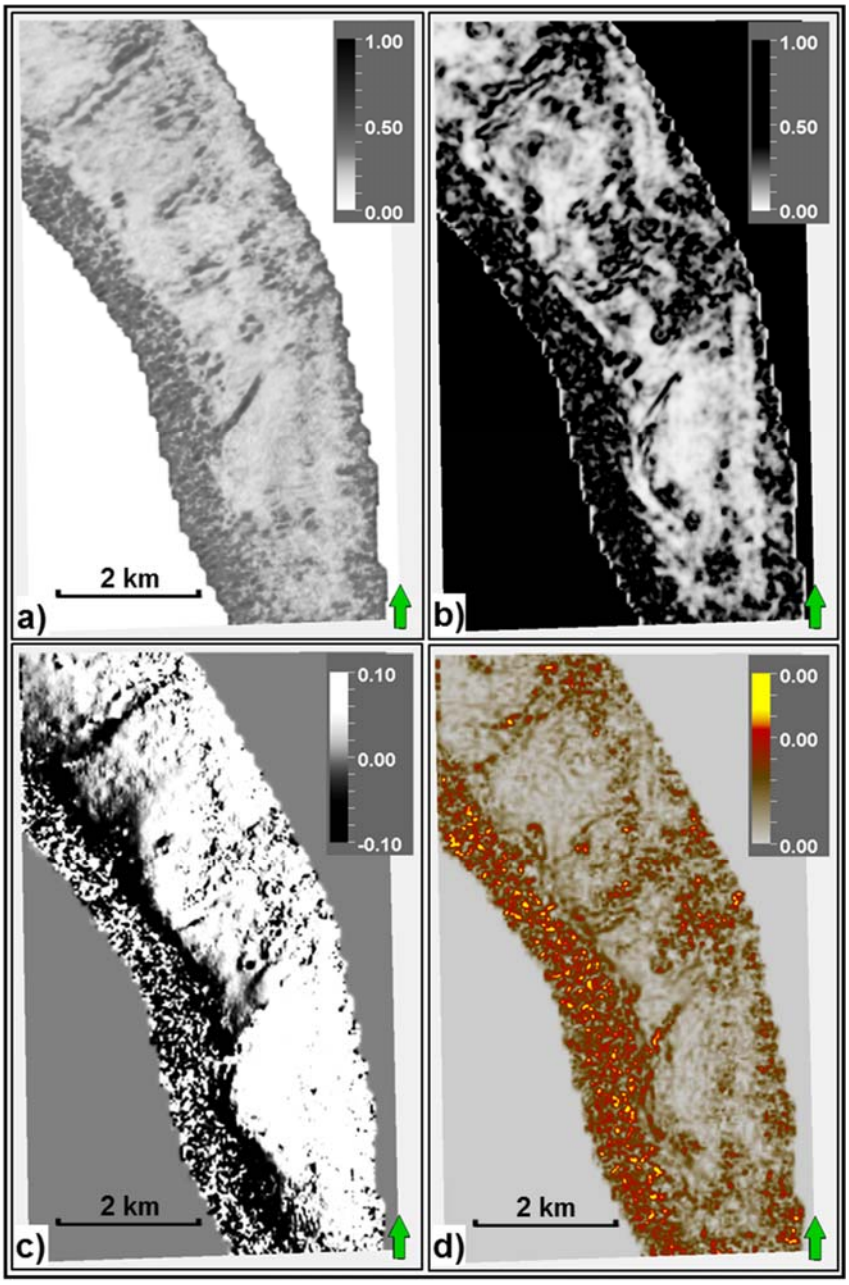

Figure 18. *An example of derived seismic volume attributes: a) amplitude contrast cube, b) chaos cube, c) consistent dip cube and d) curvature cube.*

4.2.2 Discontinuity enhancement and attribute analysis

Considering that seismic data contains a significant amount of noise, the seismic attributes require additional improvement of the signal to noise ratio. One of the most

suitable method for the faults and discontinuity identification is the so-called ant-tracking algorithm. The algorithm is based on the swarm intelligence concept (Randen et al., 2001; Pedersen et al., 2002). Generally spoken the attribute performs an edge augmentation and provides directional filters that allow the tracking of seismic discontinuities in the direction of interest. The ant tracking method is applied to the selected cubes (i.e. amplitude contrast, chaos, consistent dip and curvature - see figure 18).

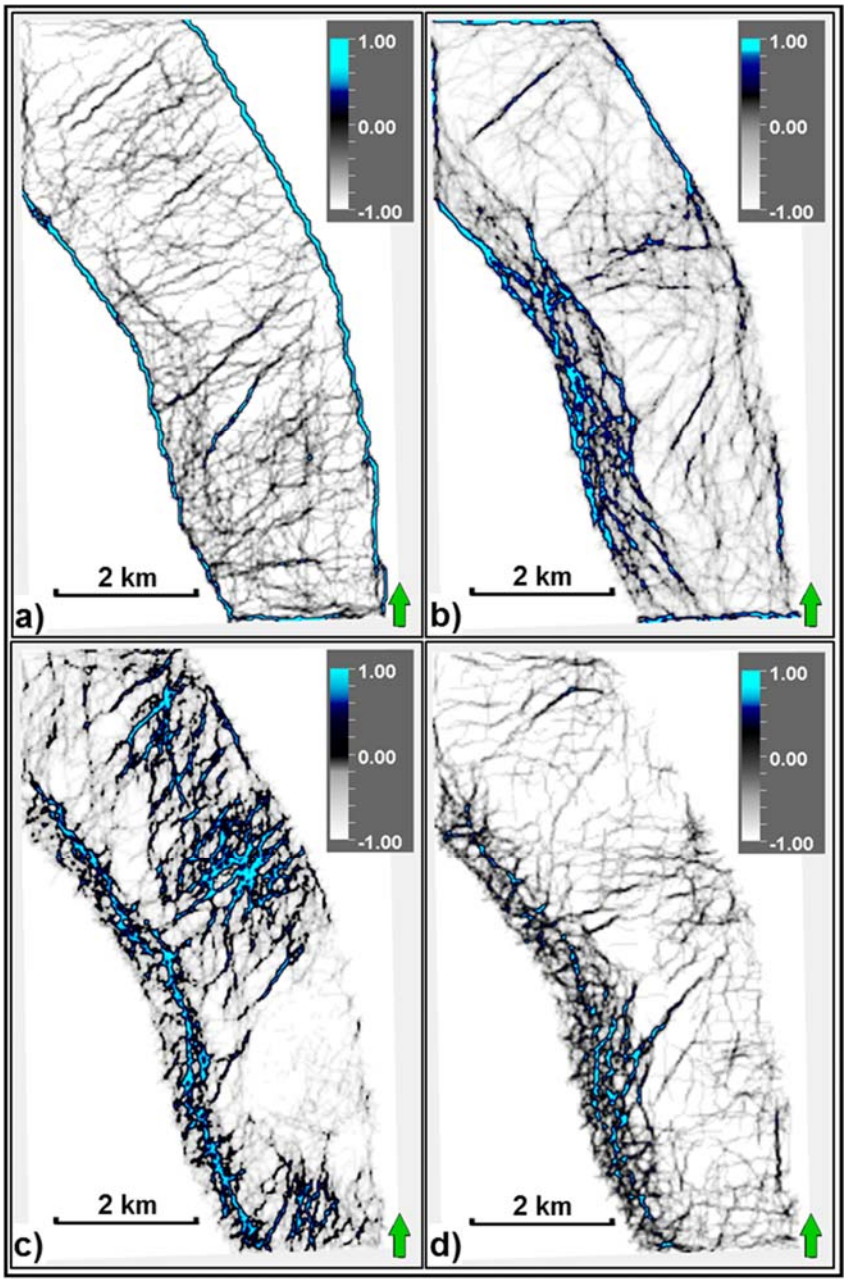

Figure 19. *An example of the applied ant-tracking algorithm to derived seismic volume attributes: a) amplitude contrast cube, b) chaos cube, c) consistent dip cube and d) curvature cube.*

The results, displayed in Figure 19 use the same time slice that is used in Figure 18. As can be observed in some areas ant-tracking cubes based on the different seismic attributes provide different fault pattern. This could be explained by the low signal-noise ratio of the seismic that makes the identification of the faults difficult.

4.2.3 Sampling attributes into the model

The attributes that show the fault pattern are sampled into the 3D grid, by assigning the amplitude values to the grid cell that is closest to the seismic sample. In order to increase the signal to noise ratio for each modeled zone, an averaged map of the upscaled model property is calculated. Figure 20 gives an example of this method applied to the ant-tracking attribute. The original ant-tracking cube is shown as reference in Figure 20a. It can be observed that the averaged upscaled attribute (Figure 20c) shows the faults clearer compared to the upscaled property (Figure 20b).

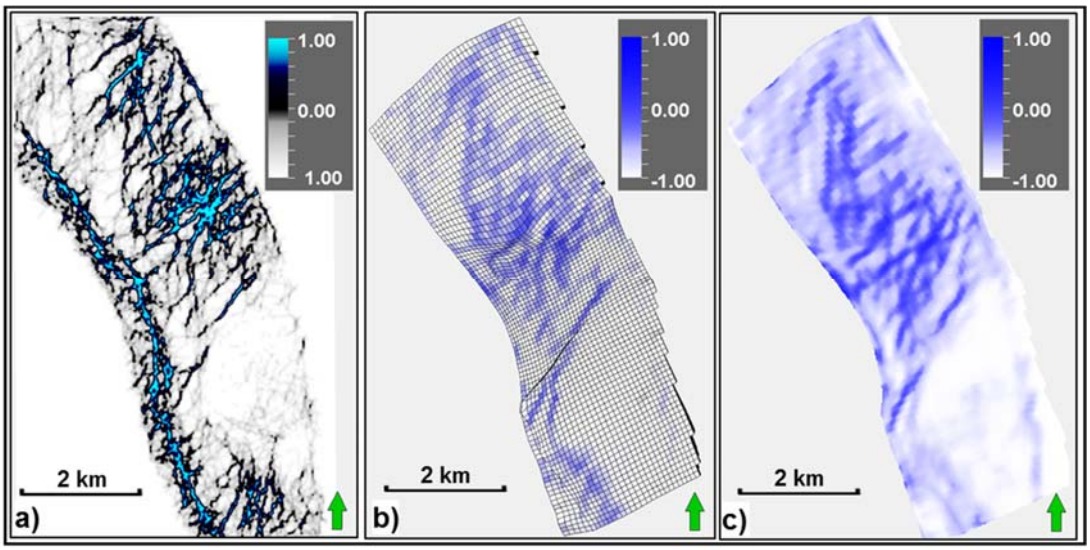

Figure 20. *An example of averaging the ant-tracking attribute: a) ant-track attribute, b) sampled attribute into 3D grid and c) average map.*

4.2.4 Derivation of fracture intensity from seismic attributes

As discussed, seismic attributes can be used to determine the fracture drivers, by capturing the changes in seismic amplitudes that are in turn associated with the faults or fracture corridors. The resultant model properties represent only variations of the

seismic attribute amplitudes and therefore cannot directly be employed as fracture intensity. However they can be used as secondary input for the interpolation of the fracture. The preferred interpolation algorithm is collocated co-kriging because one has full control over the radius of influence of the well data via the variogram ranges. In addition the influence of the secondary input, the seismic attribute, is controlled via its correlation factor with the well data. Figure 21 shows an example of the original secondary input derived from an seismic attribute (Figure 21a), together with the intensity model based on collocated co-simulation using a low correlation coefficient (Figure 21b) and high correlation coefficient (Figure 21c). In this study the calculated correlation coefficient between the measured upscaled fracture intensity and the seismic attribute is very low. However for modelling the intensity, a large correlation coefficient is used because the underlying assumption is that the fractures are associated with the fault pattern. Consequently, in the vicinity of the fault pattern a high fracture intensity is expected.

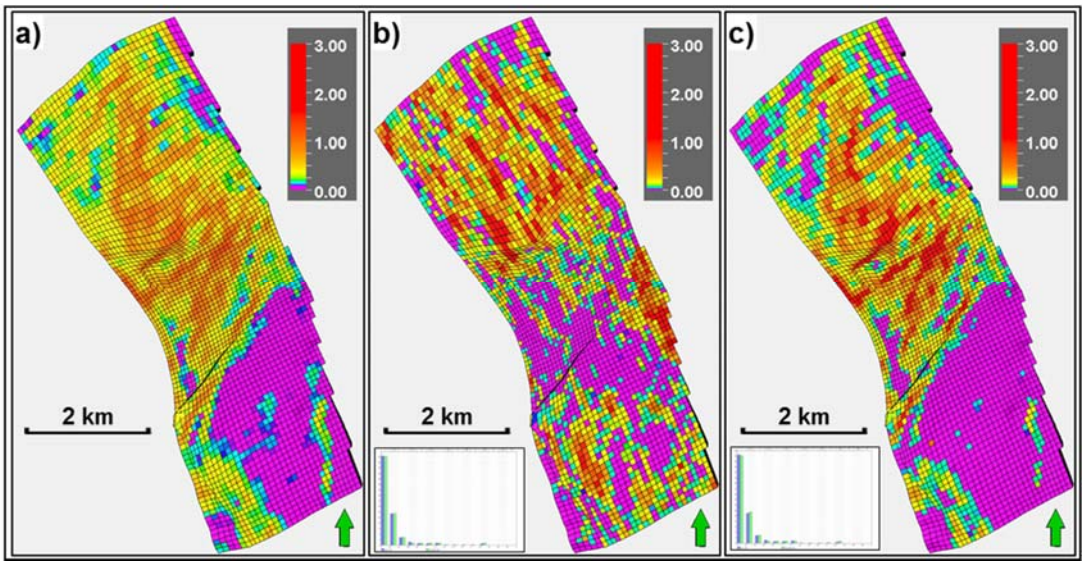

Figure 21. *An example of the correlation coefficient influence on collocated co-kriging method: a) secondary input, b) low correlation coefficient and c) high correlation coefficient.*

The other controlling factor is the variogram model. In section 4.1.3, the importance of variogram modelling has been discussed. The secondary input provides sufficient amount of points that allows a reliable variogram modelling. The variogram parameters are derived from these secondary properties assuming that the relation between fracture intensity and the seismic attributes is plausible. Figure 22 shows two different

variogram models for the secondary inputs of the attributes consistent dip (22a) and chaos (22b). As can be observed, using a large correlation coefficient the intensity property is largely influenced by the secondary input, which reduces the influence of the variogram range to the area around the wells (data points).

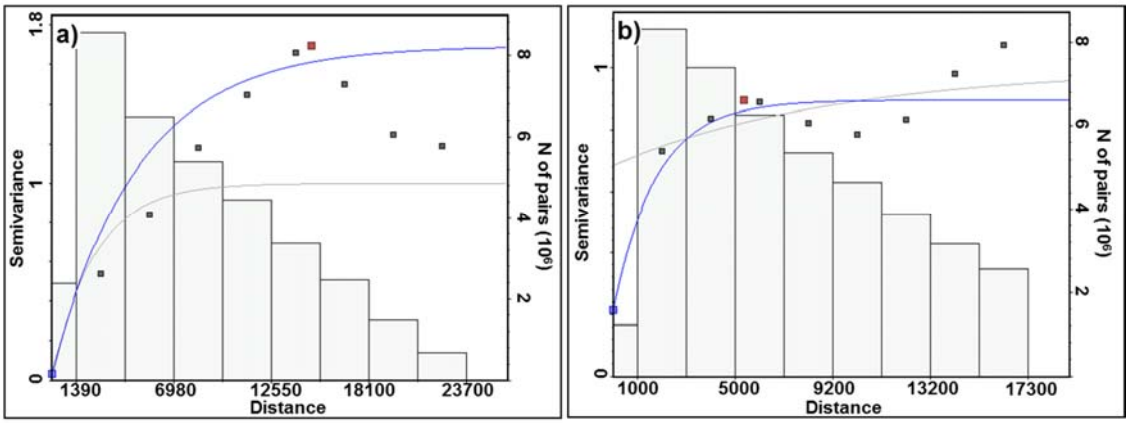

Figure 22. *An example of the variogram models generated from the secondary inputs (seismic attributes) for: a) consistent dip and b) chaos.*

4.3 Estimation of the reservoir properties

The estimated fracture properties are used in order to generate the fracture network models. Several DFN models are generated using the same fracture parameters (e.g. length, aperture and orientation) guided by different intensity models. The fractures are upscaled into the reservoir model in order to derive the fracture based reservoir permeability. In general, the process involves the assignment of the fracture properties to the each model cell. For the fracture permeability, two different upscale methods are available. The flow based method uses a simulation technique based on the Darcy equation and takes into account the complete geometry and the fracture connectivity as filtration pathways. This method delivers accurate results, however it is very CPU demanding. An alternative approach is the so called ODA method. The method is based on a statistical model, assuming that all fractures within the grid cell contribute to the grid cell permeability without taking the fracture connectivity into account (Decroux and Gosselin, 2013; van der Most, 2008). The results of upscaling procedure are presented in form of the permeability property for the three main directions X, Y, Z.

4.3.1 Evaluation of the reservoir properties

In general, naturally fractured reservoirs are considered as dual flow models with contribution of the rock matrix and the fractures (Nelson, 2001). From the viewpoint of flow simulation, the main pathways are provided by the fractures while the matrix influence is often neglected. Given that, the model comparison based on the upscaled fracture permeability appears to be a suitable approach. The method compares the models via their permeability distribution and cumulative probability distributions characterized by their P10, P50 and P90 values, Figure 23. In addition, the connectivity of the areas showing high permeability above a selected threshold value is analyzed. The connectivity analysis is done for a number of pseudo wells considering areas of connected volumes that are connected to the pseudo well under consideration. This allows attaining insight into possible high flow zones linked to the selected pseudo well. Figure 24 shows the location of the pseudo wells (24a) and an example of the connected high permeability zone linked to the pseudo well 4 (24b).

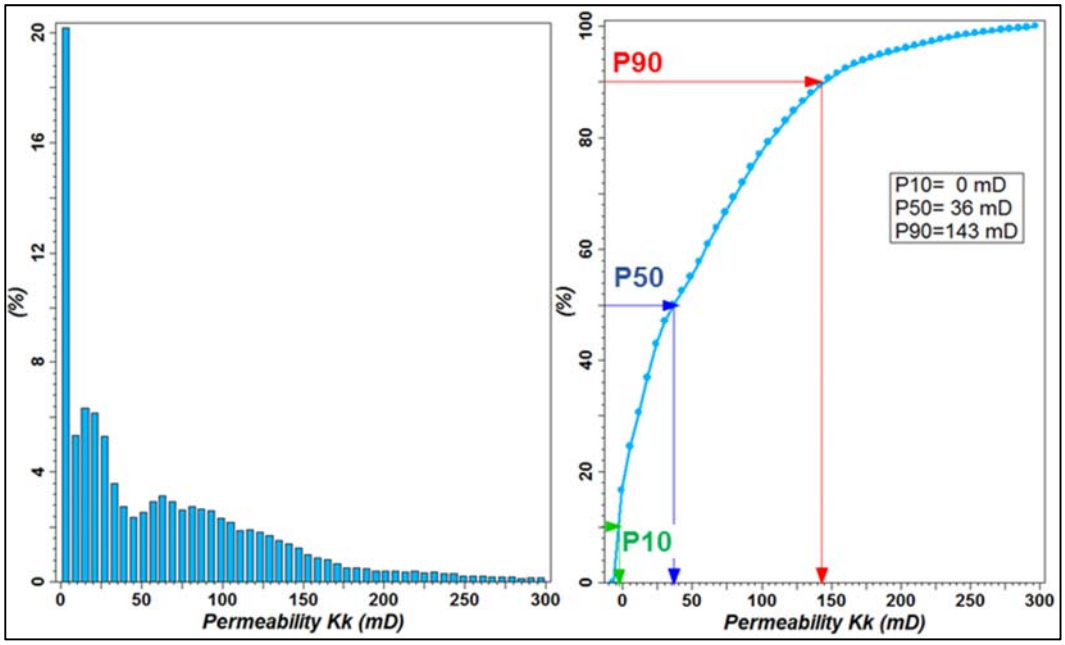

Figure 23. *Evaluation of a fracture model: histogram of permeability (left) and cumulative distribution function (CDF) with P10, P50 and P90 values (right).*

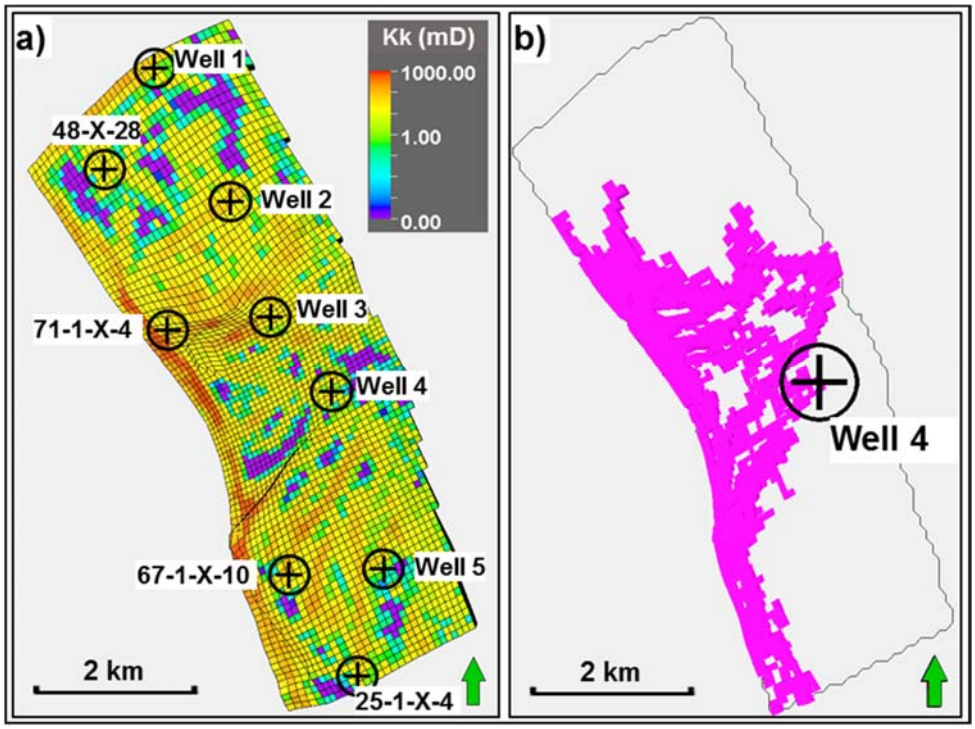

Figure 24. *Evaluation of the results: a) the location of the provided and pseudo wells and b) example of connected volumes in well 4 for the high permeability.*

5. Results

5.1 Analysis of statistical laws

The following section discusses the statistical laws used in fracture modeling for simulating fracture length and fracture aperture. The equations are shown in Table 2, chapter 4.1.2. Since fracture intensity does not affect the parameter distribution, the analysis uses a constant low intensity of 0,005 ft^{-1}. As the same statistical laws can be applied to fracture length, aperture or permeability, the discussion is focusing on fracture length. The distributions described by laws are provided on the histograms (Figure 25-28). It is worthwhile mentioning that the input parameters are displayed in the green boxes, while the statistic of the simulated fracture length is given by the blue boxes. In this way, one can observed the ability of the laws to simulate desired properties.

Normal distribution

The normal distribution is often used in natural sciences. The distribution is symmetric and represented by a bell shaped density curve. Two factors control the distribution: the mean value determining the density peak, and the standard deviation, which controls the spread of the distribution curve.

Figure 25 illustrates the impact of changing the mean and standard deviation on the normal distribution. One can notice that changes in the mean length only affect the position of the distribution peak, Figure 25a, b. The typical symmetric shape of the distribution remains unaffected. Variations in the standard deviation affect the distribution shape. An increase in the standard deviation delivers a wider distribution, Figure 25c, d.

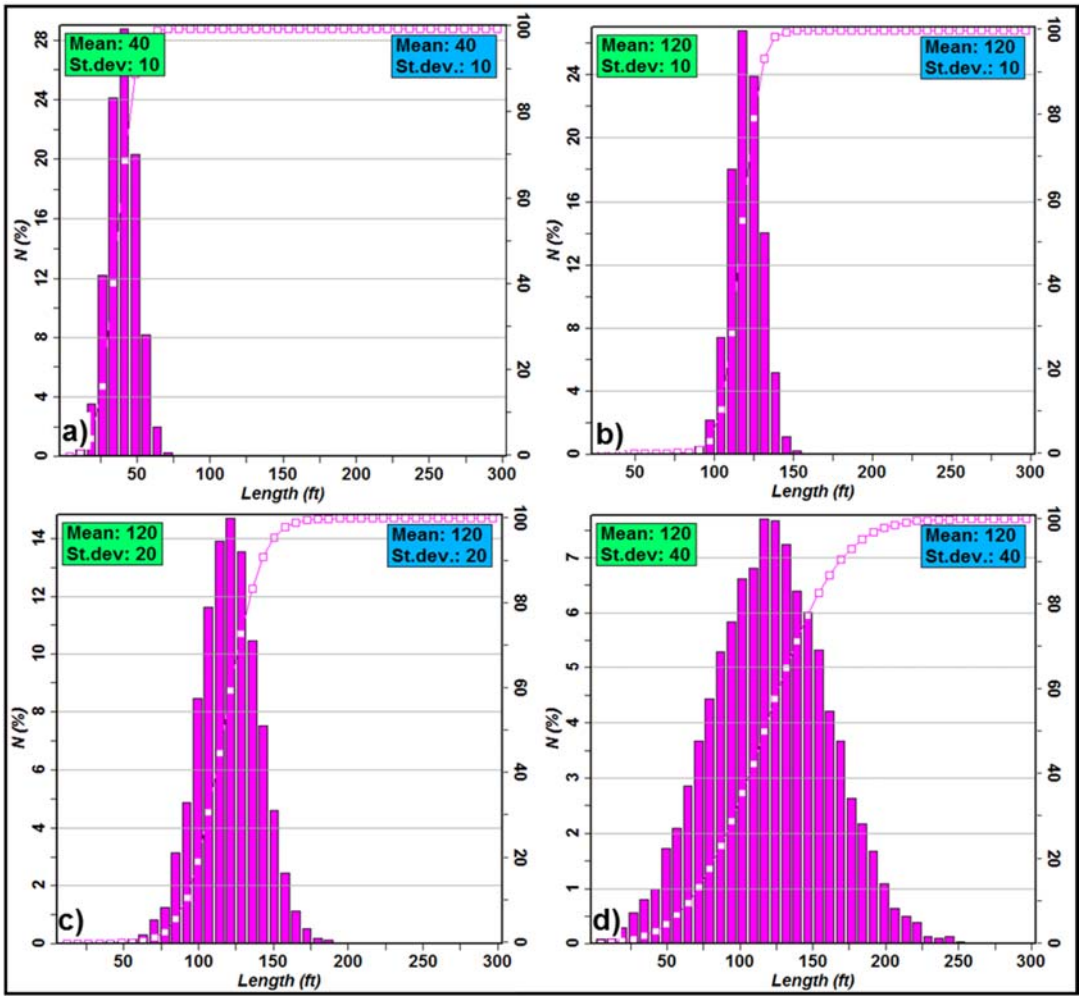

Figure 25. *Normal distribution of fracture length presented by histogram and CDF (pink line). Distribution changes as the result of variation in: a) and b) the mean value, c) and d) the standard deviation.*

Log normal distribution

The log normal distribution is closely related to the normal distribution. In general, it is characterized in terms of a log transformed variable using the same parameters as a normal distribution, mean and standard deviation (Davis and Sampson, 1986). If the logarithm of a variable X is normally distributed, then the variable itself is log normally distributed. The lognormal distribution is skewed with a longer tail on the right hand side. Figure 26 shows changes in the log distribution related to the variation of the mean and standard deviation. Similar to the normal distribution, the changes in the mean value have no major influence on the distribution shape. In addition, a more

skewed shape of the distribution can be observed for larger standard deviations. For comparison, the normal distribution is displayed as a black solid line in Figure 26.

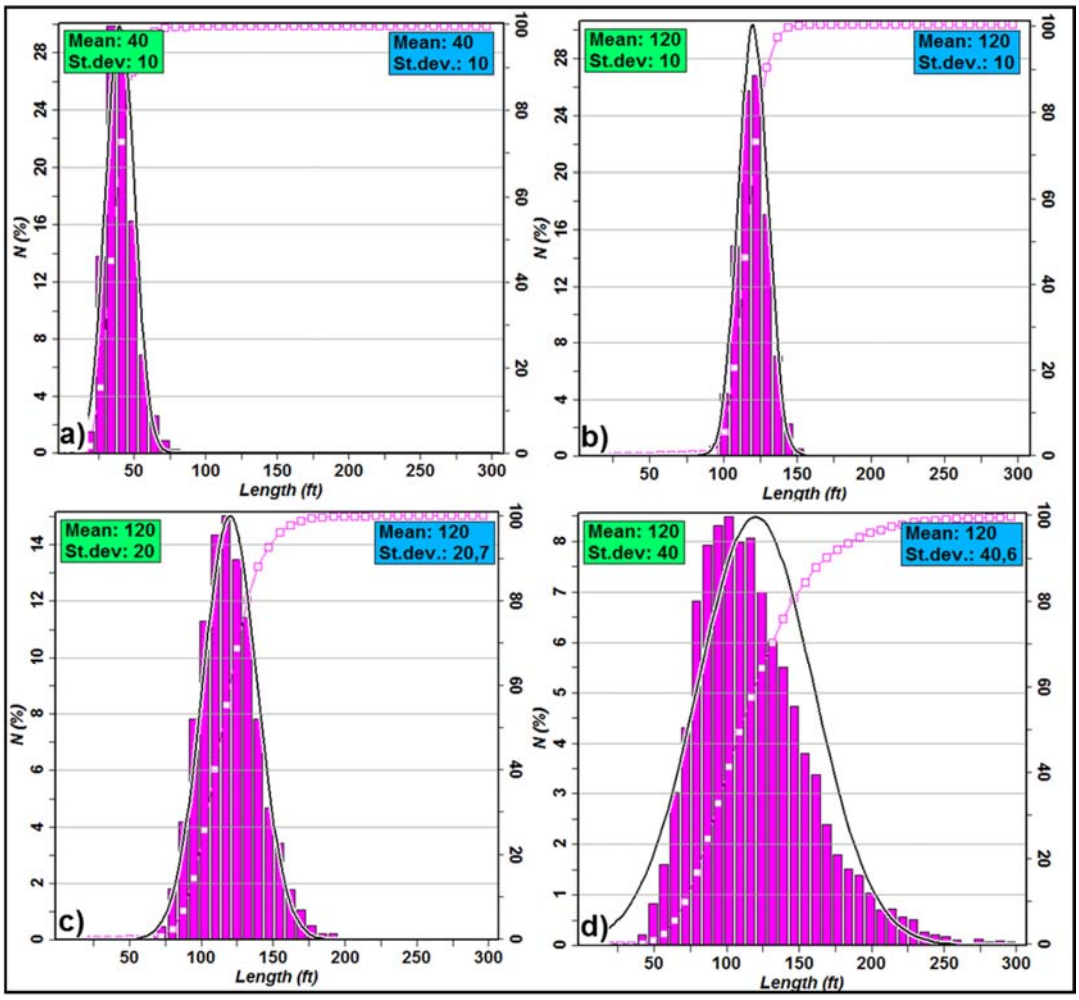

Figure 26. *Log normal distribution of fracture length presented by histogram and CDF (pink line). Distribution changes as the result of variation in: a) and b) the mean value, c) and d) the standard deviation.*

Exponential distribution

This distribution is controlled by the specific scale parameter *β* (Cowie and Scholz, 1992). The scale parameter (*β*) is numerically the mean value and at the same time the standard deviation of the distribution. Figure 27 shows the fracture length distribution based on the exponential law for different values of *β*.

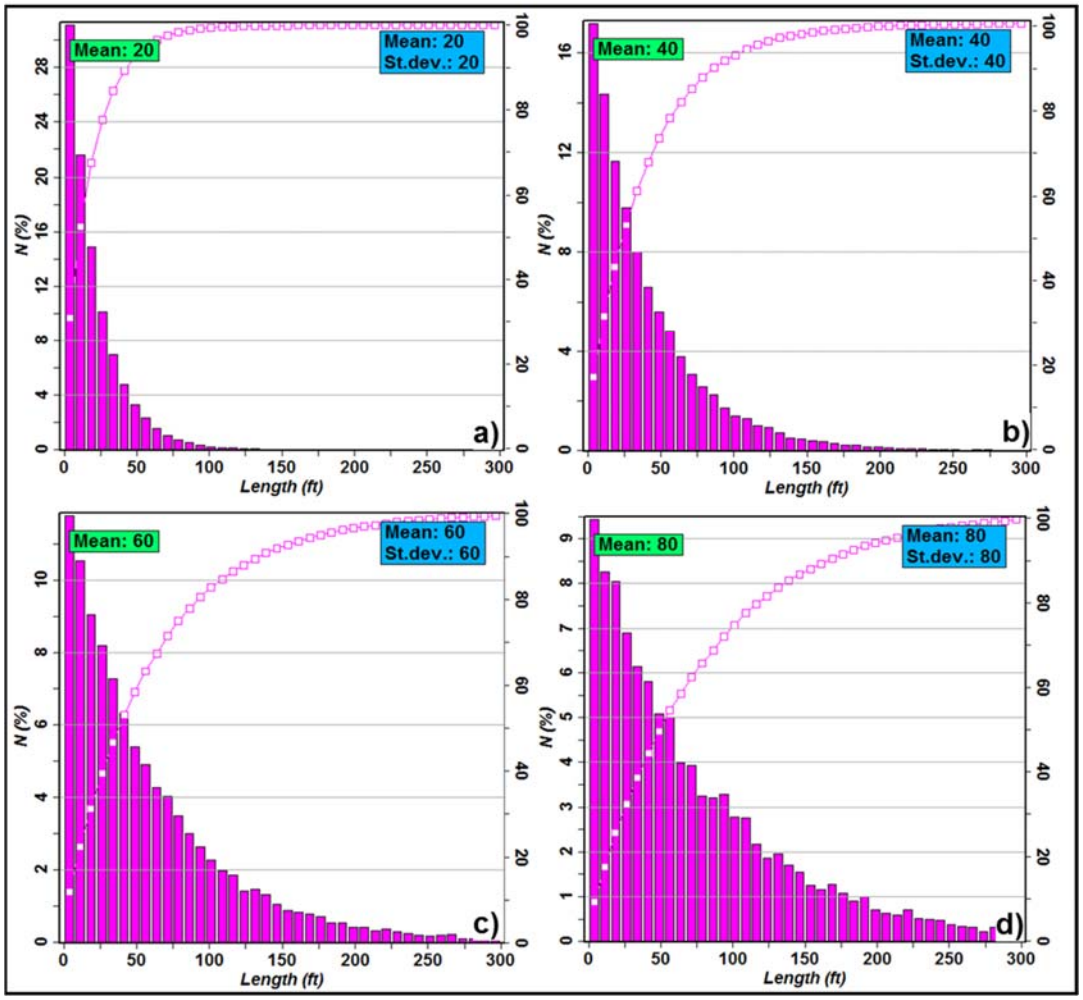

Figure 27. *Exponential distribution of fracture length presented by histogram and CDF (pink line). The four histograms show different fracture length distributions as the result of changes in the mean value.*

Power law distribution

The power law distribution has a shape similar to the exponential distribution and is controlled by a scaling parameter and an exponent. While the exponent α is controlling the spread, the scaling parameter is positioning the distribution along the length axis. When displayed on double-log scale, the power law distribution can be approximated by a straight line. Figure 28 illustrates the influence of both parameters on the distribution. A larger exponent leads to an increasing number of short-length fractures resulting in a smaller mean length (Figure 28a, b). The modeling software Petrel introduces the shape factor that is related to the exponent ($shape = \alpha - 1$). Another controlling factor is the lower limit of the distribution range (x_{min}), which is represented

by the so-called scale factor. An increase of this parameter results in a larger modeled mean length and standard deviation.

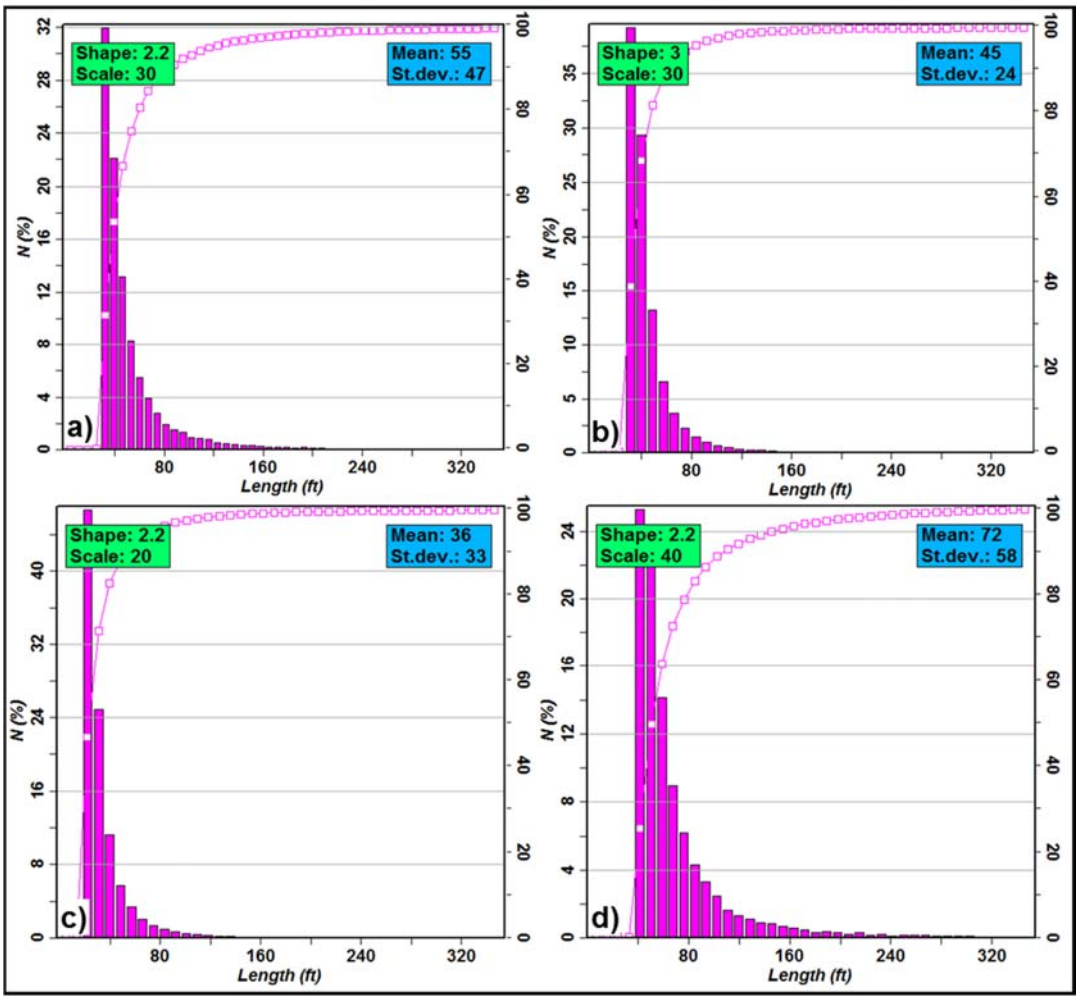

Figure 28. *Power law distribution of fracture length presented by histogram and CDF (pink line). Distribution changes as the result of variation in: a) and b) shape factor, c) and d) scale factor.*

The shape of the presented distributions suggests that the exponential and the power law describe best fracture length distributions with mainly small values. Fracture length distributions presented in the literature often reveals a similar pattern (La Pointe et al., 2002; Thachaparambil, 2015; Wilson et al., 2015) and thus either of these two laws usually best describe the fractures. The power law is often used to describe the fracture aperture-length relation and the aperture-permeability relation. In order to summarize the distributions commonly used in fracture modeling, all distributions are plotted in Figure 29. It should be noted that this comparison is based on the same

modeled mean values, standard deviation and fracture length range applied to all distribution laws. The plotted distributions show some similarities, for instance, the exponential and the power law distribution show the largest number of fractures for small fracture lengths.

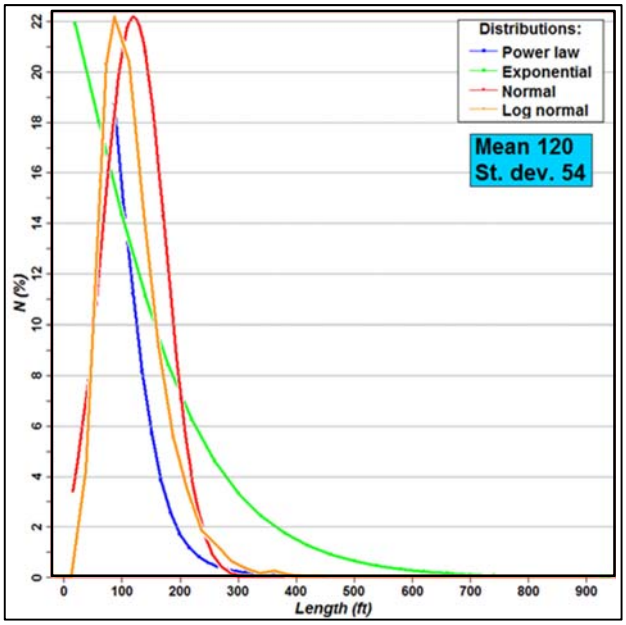

Figure 29. *The summary plot of the statistical laws. The plot shows all distributions and their relationship with respect to the same modeled values.*

5.2 Sensitivity analysis and modeling parameters

5.2.1 Sensitivity analysis

A sensitivity analysis is performed in order to investigate the impact of the essential fracture parameters on the upscaled permeability. Three sets of parameters are defined as low, base and high case: fracture length, aperture and orientation (Table 3). The modeling of these parameters is discussed in chapter Methodology, section 4.1.2. The fracture orientation, inferred from well data, is described in terms of the mean dip angle and azimuth. In this study, the fracture orientation is modeled by the Fisher distribution, mainly because of the simple of this algorithm. The sensitivity analysis of the azimuth is done via the concentration factor while the dip is hold constant.

The fracture length is derived from the outcrop studies of the Tensleep sandstones (La Pointe et al., 2002; Wilson et al., 2015). The studies are based on observations of

the Tensleep formation exposure in the Fremont Canyon area (La Pointe et al., 2002) and Circle Ridge field (Wilson et al., 2015). These studies agree upon the power law distribution of fracture length, but they provide different mean length values that vary from 40 ft (Wilson et al., 2015) to 160 ft (La Pointe et al., 2002). Consequently, the two length distributions are assumed as low and high case, respectively. The mean length for the base case is taken as the average value of the low and high case.

The dimensions of the fracture aperture can be derived from the fracture logs. It is worth noticing that only well 67-1-X-10 provides measurements of the electrical and hydraulic aperture. These measurements deliver a mean aperture value of the order of 10^{-3} ft. Additional data is inferred from published studies (Schwartz, 2006; Wilson et al., 2015). Schwartz (2006) analyses the aperture from FMI logs of the Teapot Dome and proposes a mean fracture aperture of the order of 10^{-4} (0.00017 ft). Wilson et al. (2015) propose a mean aperture of 5.6×10^{-6} ft. The different mean aperture values are modeled by the exponential law and represent the high, base and low case respectively, Table 3.

Table 3. *Defined parameters used in sensitivity analysis*

Case/parameters	Mean length (ft)	St. deviation (ft)	Mean aperture (ft)	St. deviation (ft)	Orientation (concentration factor)
I –Low Case	40	9,48	0,000056	0,000024	10
II- Base Case	80	35	0,00017	0,00012	30
III- High case	160	58	0,0022	0,0012	50

In order to estimate the influence of each parameter on the fracture simulation, one parameter at the time is set to its low or high case value while the base case value is assigned to the other parameters. Then the fracture model is calculated. The influence of each fracture parameter under investigation is captured by upscaling the simulated fracture model for its low and high case and calculating the mean permeability. It is worthwhile noting that the permeability of all models show similar values along the I, J and K direction that represent the model axes. This can be attributed to the fact that three fracture sets of different orientations are simulated. Consequently, there is no preferred permeability direction.

Alterations of the fracture length for the different cases, deliver a variation in permeability from 4 to 20 mD. A variation of the fracture orientation, in terms of the concentration factor, reveals no significant impact on the permeability. Conversely, the fracture aperture has a very large influence on the upscaled permeability covering the value range from 0,22 mD to 14000 mD. This clearly shows the dominant influence of the aperture on the upscaled permeability compared to the other two fracture parameters. The results delivered by the sensitivity analysis are displayed in form of a tornado diagram in Figure 30. The reference line in the middle of the diagram represents the mean permeability for the model where all fracture parameters are set to the base case value. It should be noted that the diagram is truncated at 200 mD. This is necessary because the mean permeability for the aperture high case is about 10^4 mD. The high case aperture can be challenged because it delivers an extremely high permeability. Its value is provided by the fracture data set of well 67-1-X-10 and cannot be verified.

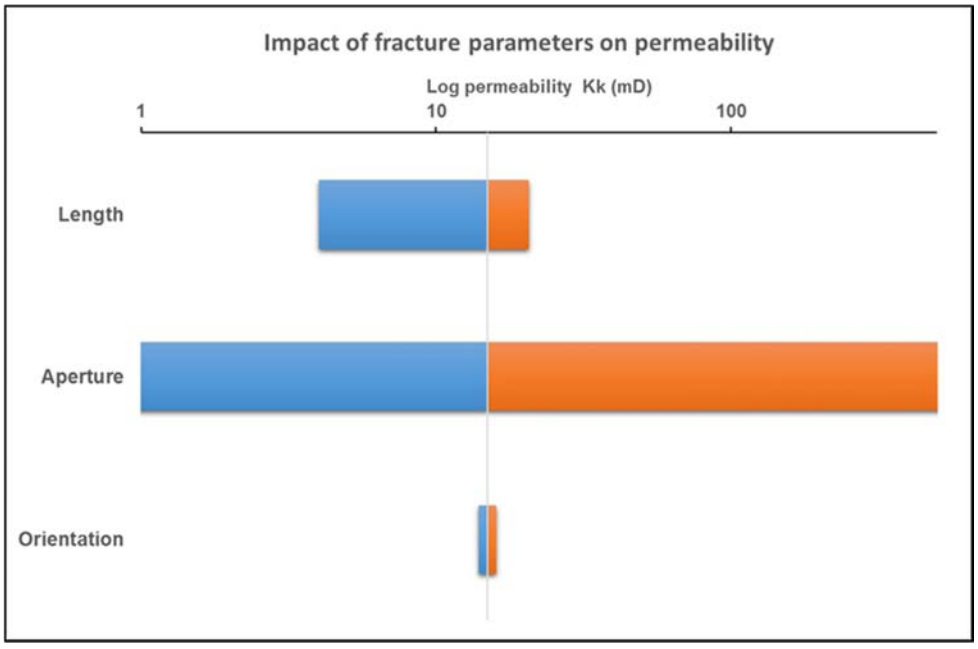

Figure 30. *Tornado chart showing the impact of the fracture parameters on the permeability in vertical (k) direction.*

5.2.2 Definition of model parameters

The final model parameters of the DFN models that result from the two modelling strategies discussed in this thesis are chosen based on the performed sensitivity

analysis. Based on inferred orientation parameters the fractures are divided into three fracture sets. The Fisher distribution based on a large concentration factor (C) with the aim to avoid wide spread of the fractures around the mean orientation integrates these sets into the models. Fracture length variations show only a minor impact on the permeability. Therefore, a cell size of 250 ft together with the high case fracture length is selected because the fracture simulation is much less CPU demanding compared to the models based on the low and base case fracture length. The power law accomplishes the modeling of fracture length. For the fracture aperture, the base case aperture is selected because it delivers a mean permeability which is comparable with the mean permeability for the reservoir published by Friedmann and Stamp (2006). The square root relation relates the fracture aperture to the fracture length. The fracture permeability is related to fracture aperture by the cubic law. Table 4 shows the fracture parameters used as input for all models based on the different approaches discussed in this thesis. Figure 31 illustrates the three fracture sets in a stereonet, the power law distribution of fracture length, and the relation of fracture aperture with fracture length and permeability, all of them used in the models.

Table 4. *The fracture parameters used in fracture models.*

Model parameters	Fracture length (ft)	Fracture aperture (ft)	Fracture orientation
Mean (ft)	160	0,00017	C=50
Standard deviation (ft)	58	0.00012	C=50
Range (ft)	0-500	0.0001-0.0016	C=50

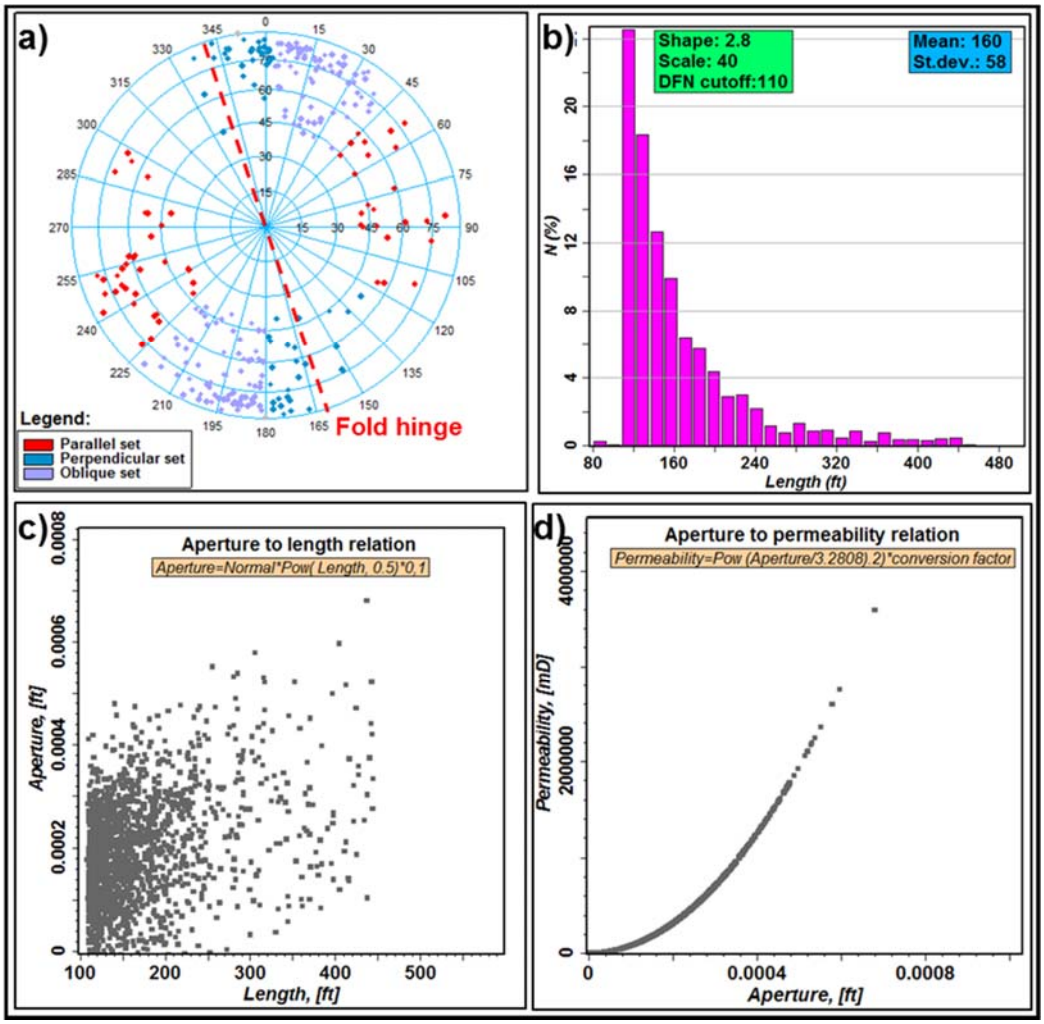

Figure 31. *Model parameters: a) stereonet with poles of the defined fracture sets together with the fold hinge, b) fracture length modeled by a power law, c) fracture aperture related to the length by the square root relationship and d) relationship between permeability and aperture defined by the cubic law.*

5.3 The standard approach in fracture modeling

As discussed earlier, the standard method uses non-conditioned interpolation algorithms for modeling fracture intensity. The variogram ranges have a major impact on the spatial distribution of fracture intensity. Therefore, three different ranges are employed in order to capture their impact on the model results (Table 5).

Table 5. *The random variogram ranges for the three cases.*

Cases	Case 1	Case 2	Case 3
Major direction (ft)	2500	6000	12000
Minor direction (ft)	2500	6000	12000

5.3.1 Fracture intensity

The fracture intensity based on Kriging and Gauss simulation are illustrated in Figure 32 for one model layer. Figure 32a, b, and c display the Kriging interpolation result for the variogram ranges given in Table 5. The remaining figures refer to the Gaussian simulation based on the same variogram ranges. The two algorithms deliver very different fracture intensity maps. For instance, the Kriging algorithm assigns the mean value of the data points to the grid cells away from the data. Accordingly, it delivers a very smooth intensity distribution. Figure 32a-c also illustrate that the variogram range controls the radius of influence of the measured data. For instance, the case with the largest range (Figure 32c) delivers the widest extent of high fracture intensity away from the data points. This can be easily observed in the south, with a fracture intensity value larger than the average value (red squares). On the other hand, the Gauss simulation (Figure 32 d, e, f) delivers a very heterogeneous fracture intensity model. The patches with low and high intensity are randomly distributed throughout the area. In addition, the dimension of these areas depends on the defined variogram ranges (Figure 32d-f).

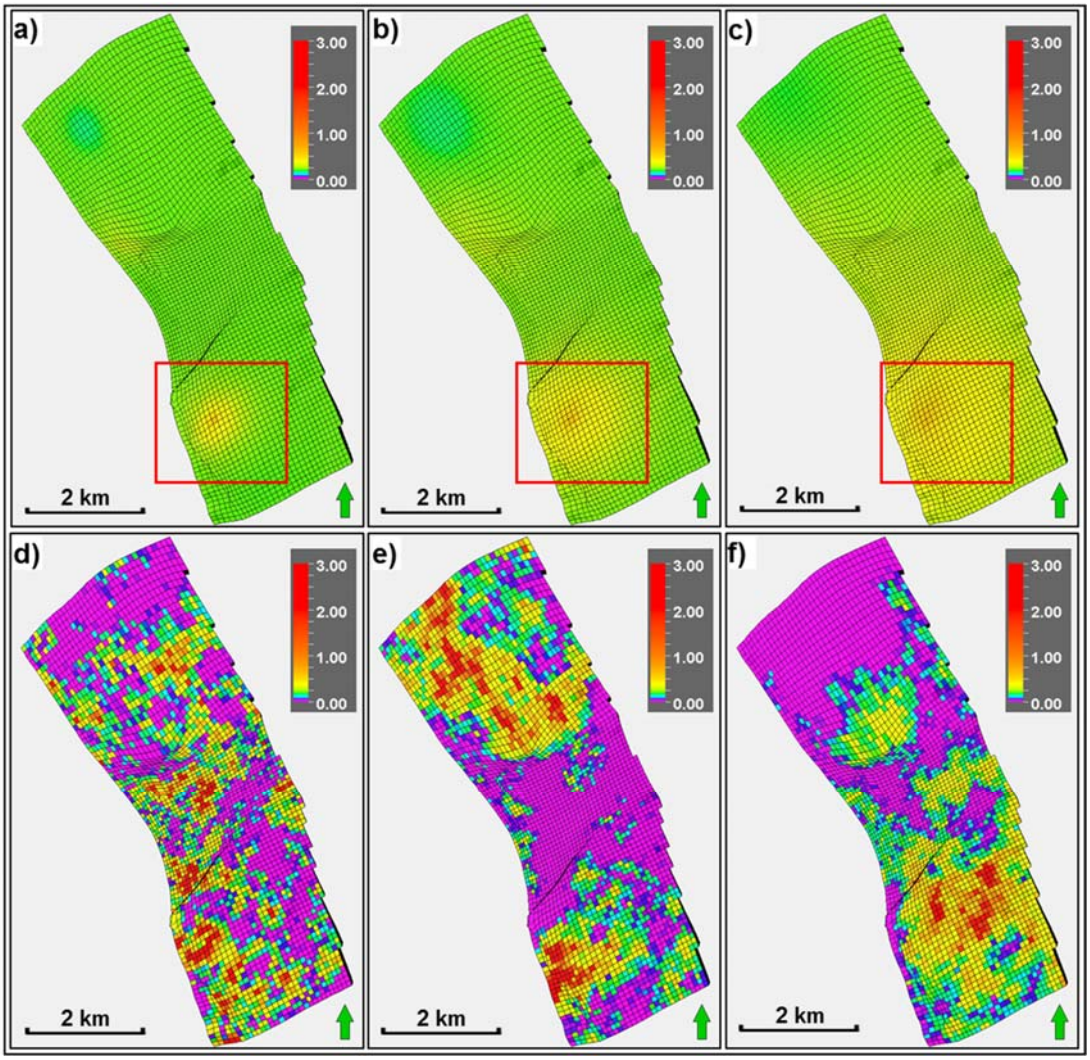

Figure 32. *Fracture intensity guided by two different interpolation algorithms for three sets of variogram ranges (cases 1-3): (a-c) Kriging and (d-f) Gauss simulation. Note the impact of the variogram ranges on the modeled results. Red squares are used to highlight the differences.*

5.3.2 Evaluation of the models

Since the permeability distribution show similarities in all three directions (i.e. I, J K), the models are further evaluated based on the upscaled permeability in the vertical direction (Kk). Figure 33 displays the permeability of the same layer and the six models discussed above. Analyzing the figures one can observe that the permeability pattern is consistent with the fracture intensity. Therefore, for the shown layer, high permeability values are absent for the models based on kriging shown in Figure 33a-c.

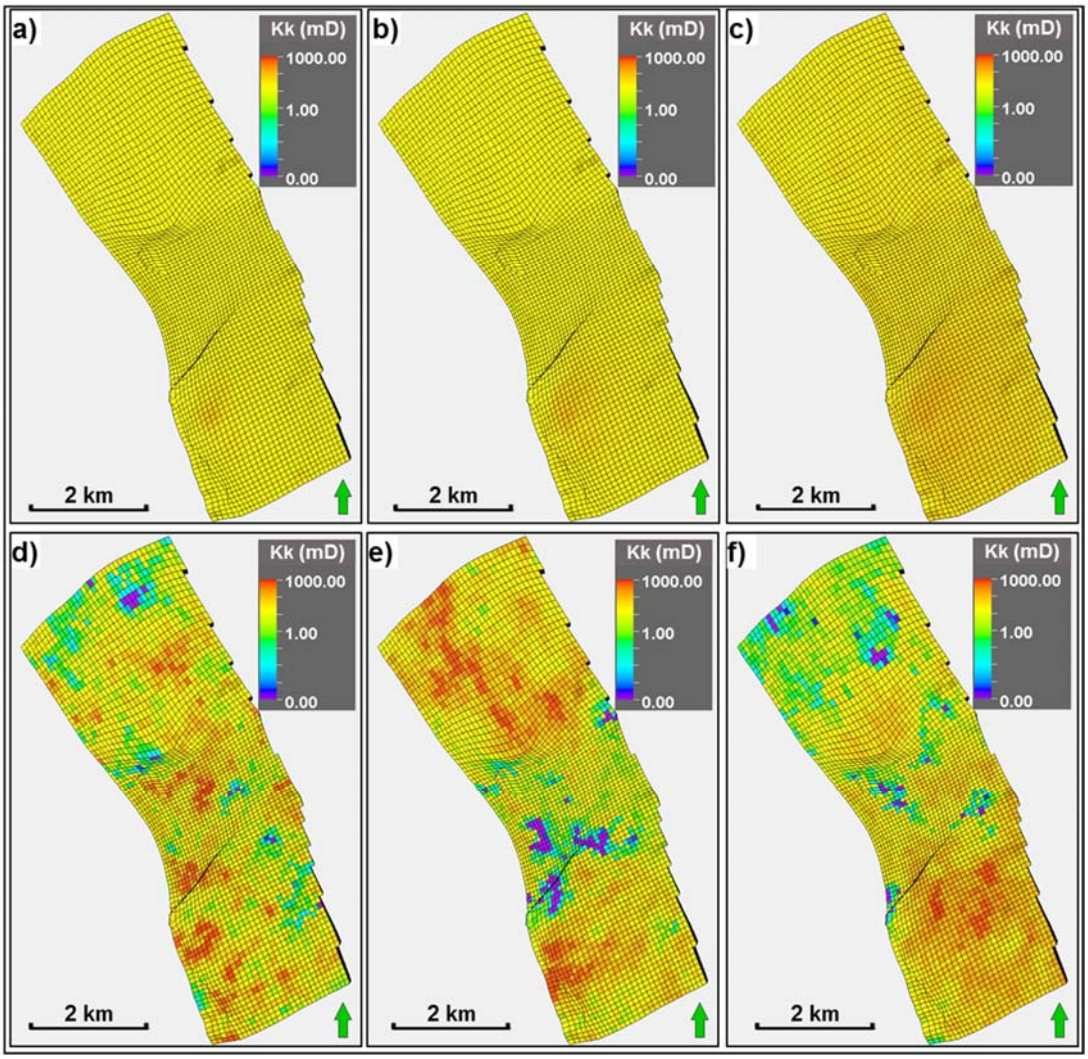

***Figure 33**. Permeability (Kk) layer of the models guided by the interpolation algorithms for the three discussed variogram cases (1-3): (a-c) Kriging and (d-f) Gauss simulation.*

Figure 33d-f show the heterogeneous permeability distribution based on the Gauss simulation. The maps display high and low permeability zones; however, the location of these zones cannot be justified. In fact, each simulation will result in a different pattern of these zones. In addition, Figure 33d-f illustrate that the variogram range controls the size of the zones of high and low permeability.

Figures 34 and 35 compare the models via their histograms, cumulative distributions, P-values and cross sections along the pseudo wells. The histogram (Figure 34a) illustrates the lognormal distribution of the permeability and emphasizes the variations between the models. Models conditioned by Kriging show more dissimilarities for the three variogram ranges. The large variogram range delivers a broader permeability

distribution by means of lower P10 and higher P90 value (dark blue) compared to a small range. Due to this wide distribution, the model displays a more heterogeneous pattern on the cross section (Figure 35c).

The models based on the Gaussian simulation show similar distributions (Figure 34 a, c), and consequently similar P-values. However, the cross sections reveal a more heterogeneous pattern in case of small variogram ranges (Figure 35a, c). It is worthwhile mentioning that both algorithms shows very similar P90 values for the large variogram range (case 3) while P10 and P50 are quite different. In addition, the Gauss based model is characterized by a larger spread of the distribution. This is because Kriging assigns the mean value to the grid cells outside the radius of influence of the data points.

A further model comparison can be performed based on the connected volumes generated for the pseudo wells. The pseudo wells are located along the anticline eastern limb in close vicinity of the NE-SW striking main faults (Figure 24a, section 4.3.1). The connected volumes incorporate only grid cells with permeability larger than the P90 value derived from the measured fracture data.

The highest dissimilarities can be observed for the wells 4 and 5 (Figure 36). The models guided by Kriging demonstrate a strong dependency on the applied variogram ranges (Figure 36a-f). An increasing variogram range yields larger connected volumes (Figure 36a-f). Also the models guided by Gauss simulation show a dependence of the variogram parameters (Figure 36g-l). A model with a small variogram range displays a far greater degree of fracture connectivity, compared to a large variogram range (Figure 36g-l).

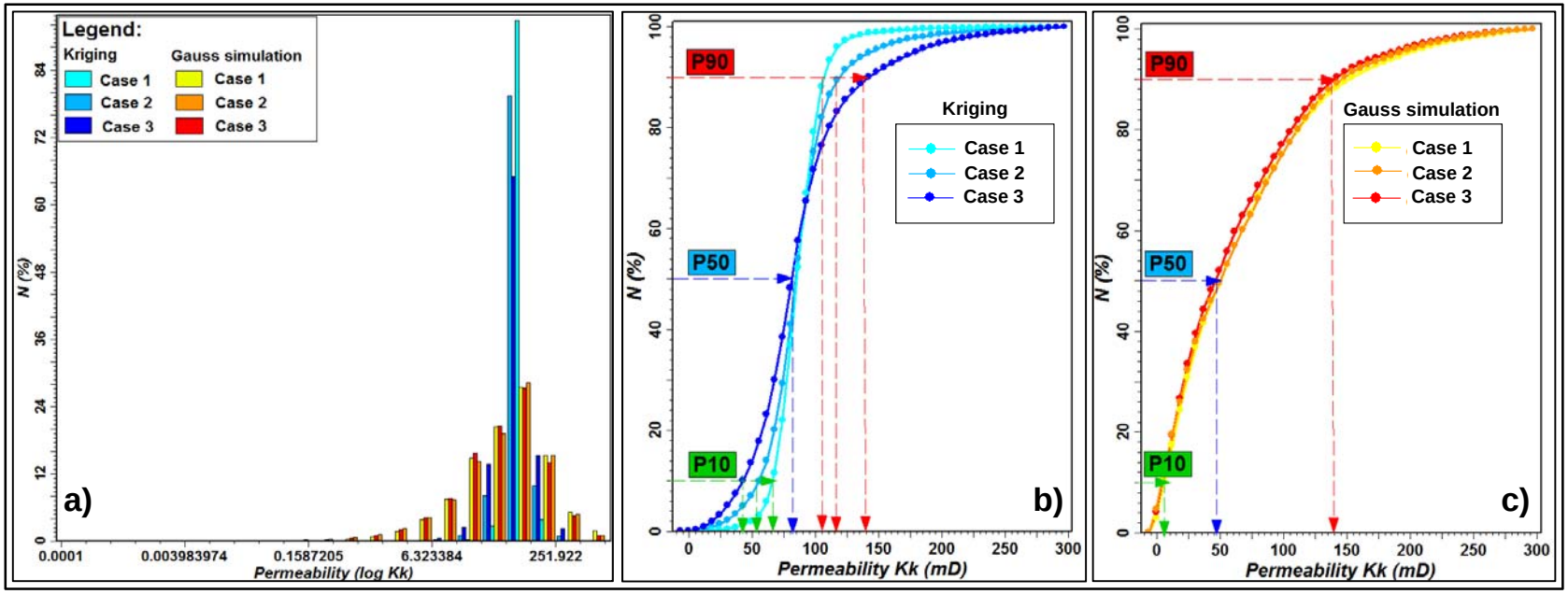

Figure 34. *The permeability distribution (Kk) for the models guided by Kriging and Gauss simulation: a) histogram of log permeability (Kk) for the generated models, b) Cumulative distribution of the permeability for the models conditioned by Kriging and c) Cumulative distribution of the permeability for the models conditioned by Gauss simulation.*

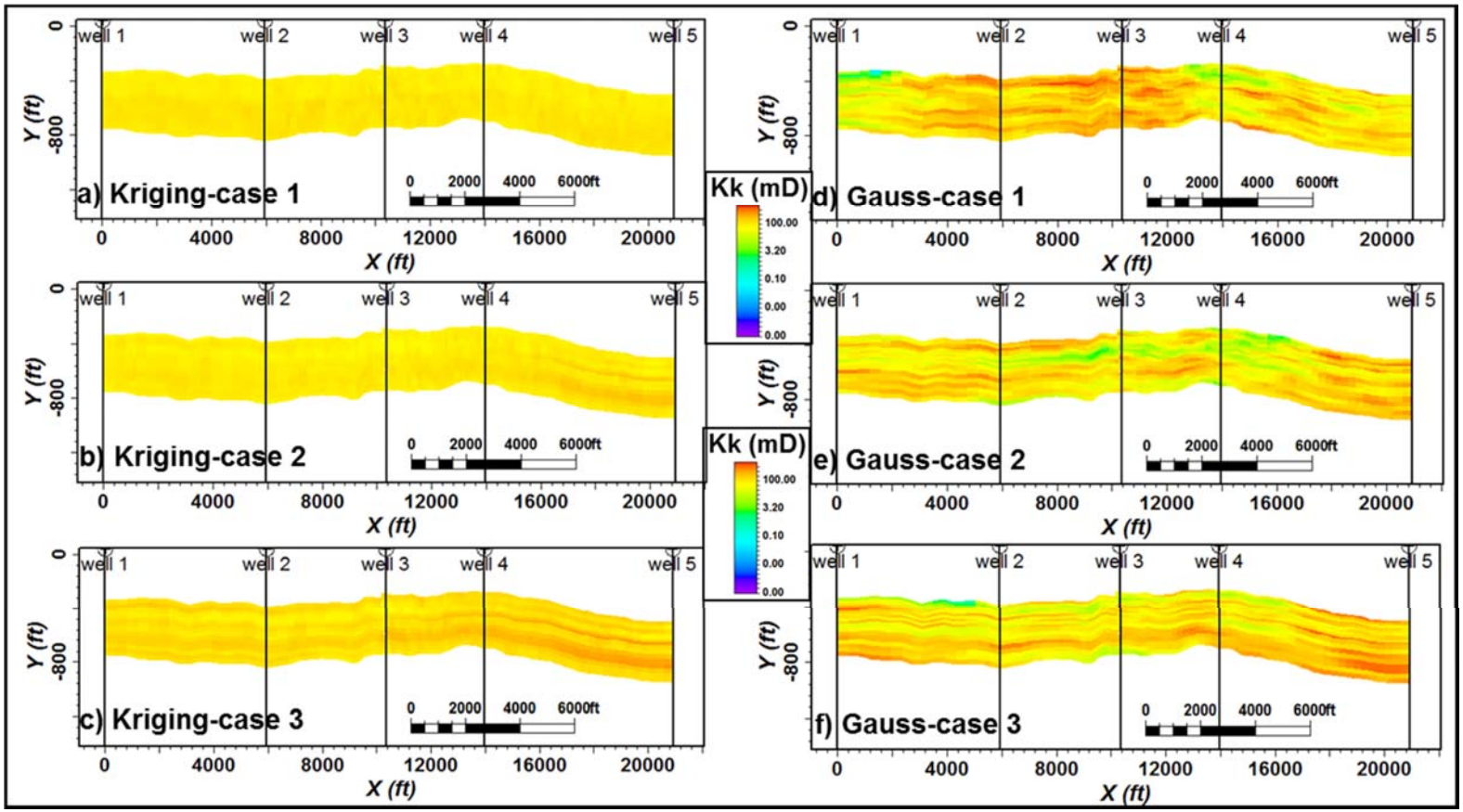

Figure 35. *The cross sections along five pseudo wells shown in figure 24 for the models guided by interpolation algorithms for the three different variogram cases: (a-c) Kriging and (d-f) Gauss simulation.*

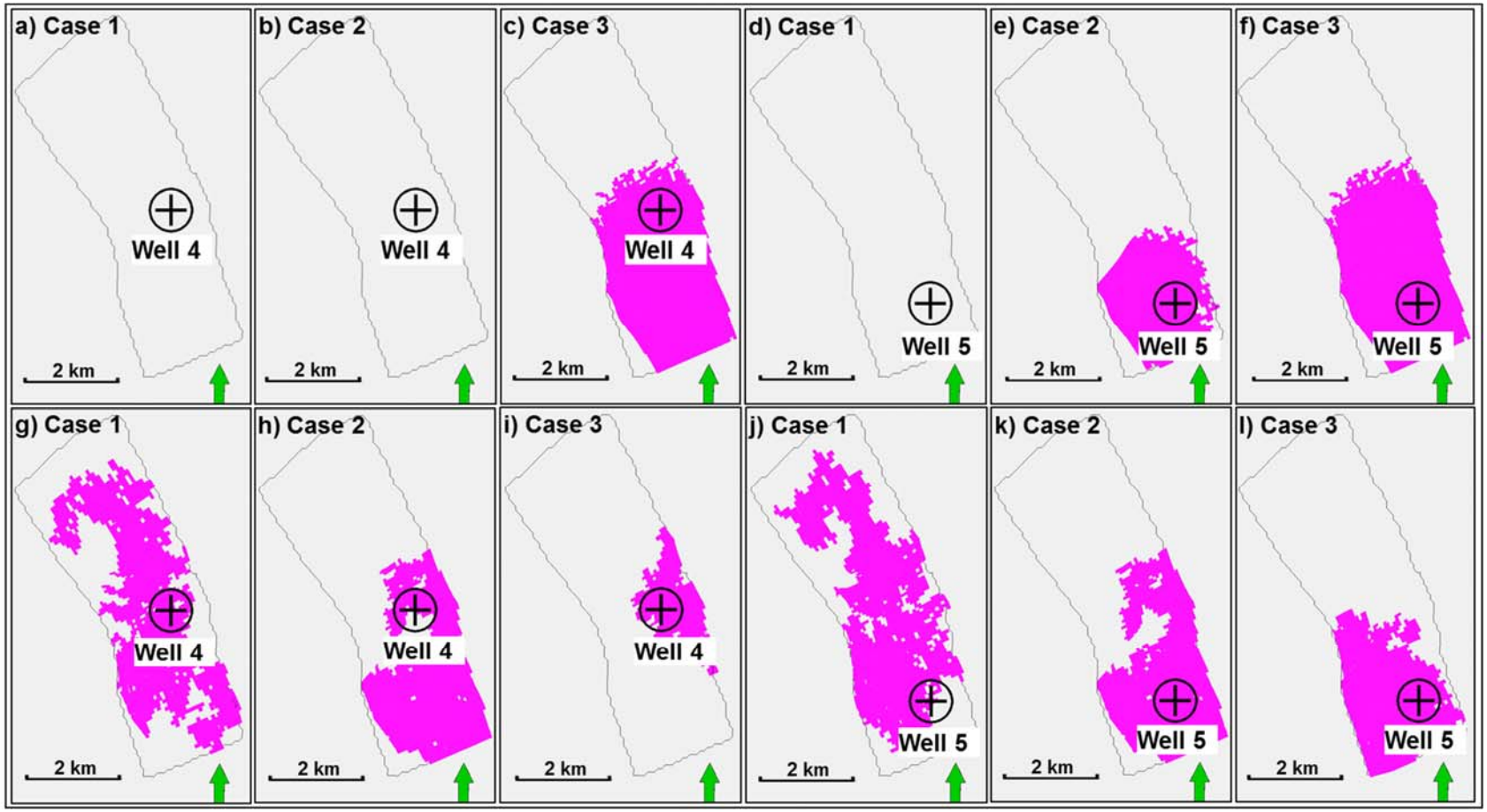

Figure 36. *Connected volumes for the pseudo wells 4 and 5, for the models based on Kriging (a-f) and Gauss simulation (g-l). For each well, the connected volumes are shown for three variogram cases (Table 5).*

5.4 Seismic attributes based approach

This section describes the usage of seismic attributes for guiding the fracture intensity distribution.

5.4.1 Variogram parameters derived from seismic attributes

The well data do not allow a correct estimation of the horizontal variogram range. Only the vertical variogram range can be inferred reliably because of the densely sampled fracture intensity logs. On the other hand, the seismic attributes provide additional data points and allow a reliable estimation of the horizontal variogram range. Assuming a close relationship between the fracture intensity and the seismic attributes, the horizontal variogram range is derived from the seismic attributes sampled into 3D grid. This variogram range is used in collocated co-kriging to interpolate the fracture intensity using a seismic attribute as secondary property (see the chapter Methodology, section 4.2.4). In order to maintain the pattern displayed by the seismic attributes a large correlation coefficient between the measured fracture intensity and seismic attribute is chosen in collocated co-kriging. The used variogram ranges are given in Table 6. The results are discussed in the following sections.

Table 6. *The variogram parameters used in collocated co-kriging process.*

Attributes	Amplitude contrast	Chaos	Curvature	Consistent dip
Major direction (ft)	4693	5615	5590	14000
Minor direction (ft)	2200	1555	3908	5500

5.4.2 Fracture intensity

The fracture intensity models are displayed for a layer of the 3D grid in Figure 37. The four maps correspond to the seismic attributes amplitude contrast, chaos, curvature and consistent dip. The maps show quite different intensity patterns. In the southern area, the maps a and b show a significantly different pattern compared to the maps c and d. In addition, the models guided by chaos and curvature (Figure 37b, c) deliver a high fracture intensity along the fold hinge. This pattern is not observed in the other

two models. In addition, the models in Figure 37b and c display a low fracture intensity in the northern area. The models guided by amplitude contrast and consistent dip (Figure 37a, d) deliver a high fracture intensity in this area. However, all maps share some similarities. In general, they display higher intensities in the vicinity of the faults along the eastern limb. Also, in the central part the maps display a similar fault pattern (black squares). The fracture intensity varies within the area from medium to high depending on the model.

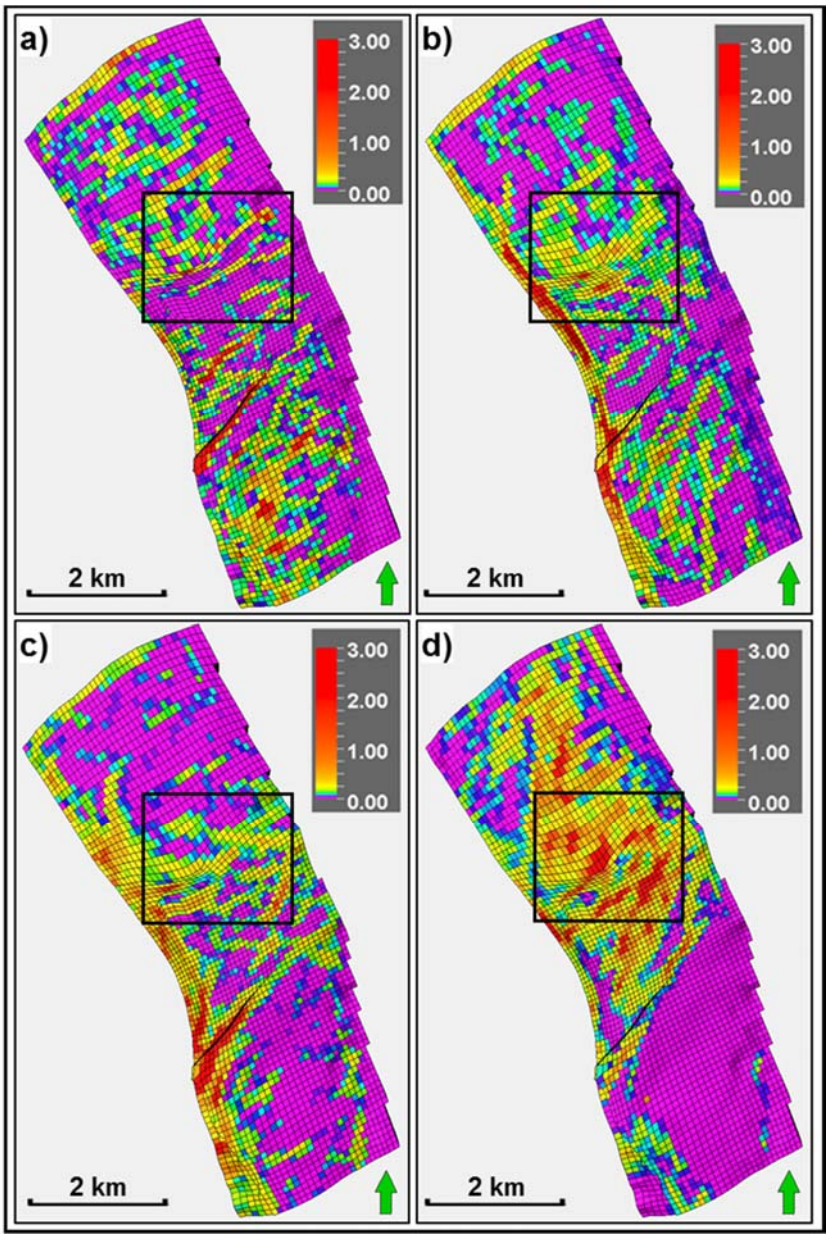

Figure 37. *The fracture intensity maps for the models based on different seismic attributes: a) amplitude contrast, b) chaos, c) curvature and d) consistent dip.*

5.4.3 Evaluation of the models

The models are further evaluated using the upscaled permeability. Figure 38 displays the permeability properties for one layer of the models conditioned to the seismic attributes shown in Figure 37.

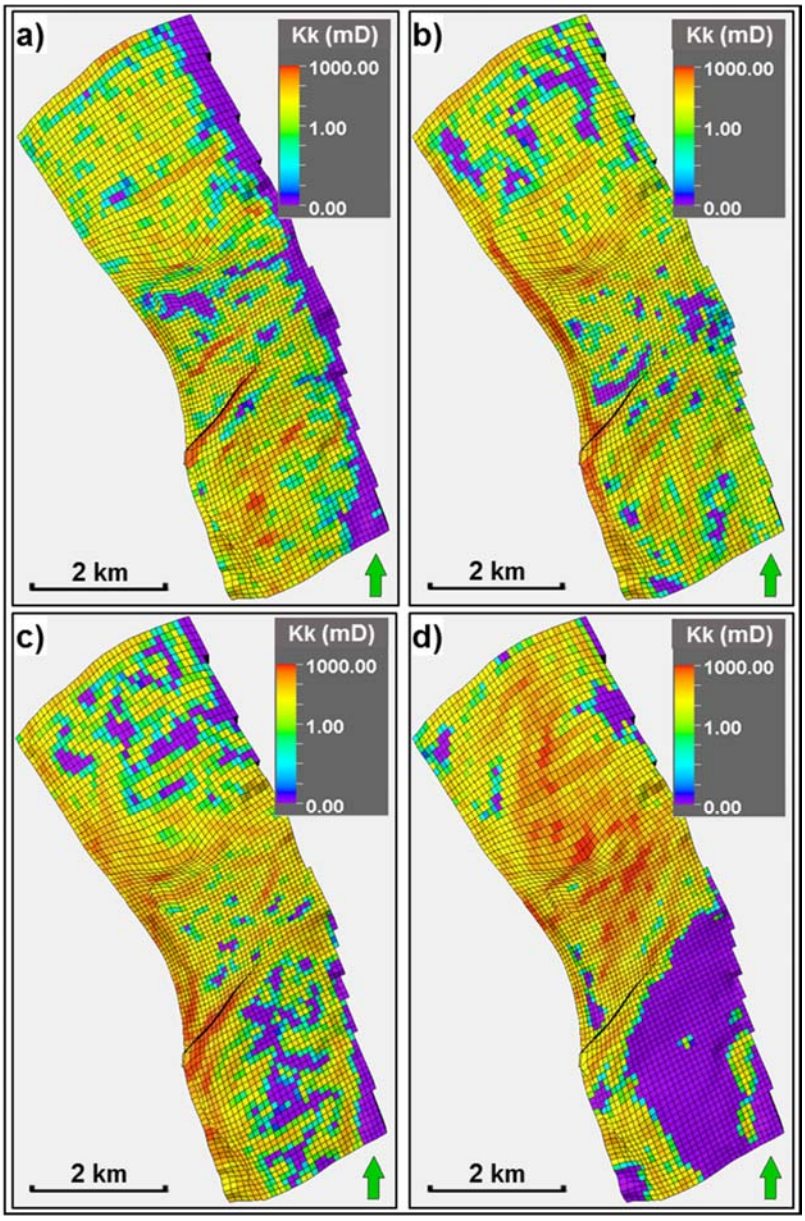

Figure 38. *The permeability (Kk) maps for the models based on different seismic attributes: a) amplitude contrast, b) chaos, c) curvature and d) consistent dip.*

A comparison of figures 37 and 38 shows that high permeability zones are in accordance with high intensity zones and vice versa. In general, higher permeability

zones are closely related to the main structures of the area. Also, similar to the intensity models, only the chaos and curvature based models reveal higher permeability zones along the fold hinge.

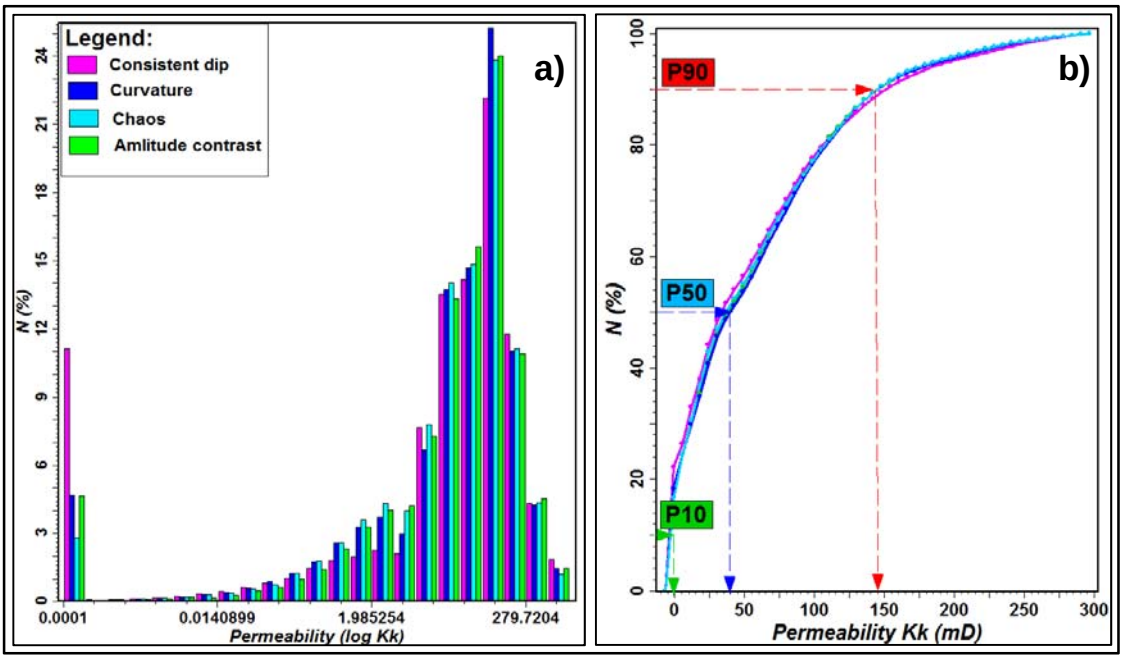

Figure 39. *The permeability (Kk) distribution for the models based on different seismic attributes: a) histogram of log permeability (Kk) for the generated models, b) Cumulative distribution of the permeability of the models conditioned to the seismic attributes.*

Figure 39 provides insight into the permeability distribution through the histograms, cumulative distributions and characteristic P-values. The histograms display similar permeability distributions for all models conditioned to the different seismic attributes (Figure 39a). Also the cumulative probability distribution confirms the similarities between the models. Consequently, the P-values (P10-P50-P90) do not deviate between the four models (Figure 39b). A further comparison of the models is provided by cross sections. Figures 40 and 41 show the cross sections along the pseudo wells and the provided wells, respectively. The cross sections show patches of high permeability above 100 mD. They are linked by zones of lower permeability (1-50 mD). In addition, the model based on consistent dip (Figure 40d) shows a very low permeability zone in the southern part.

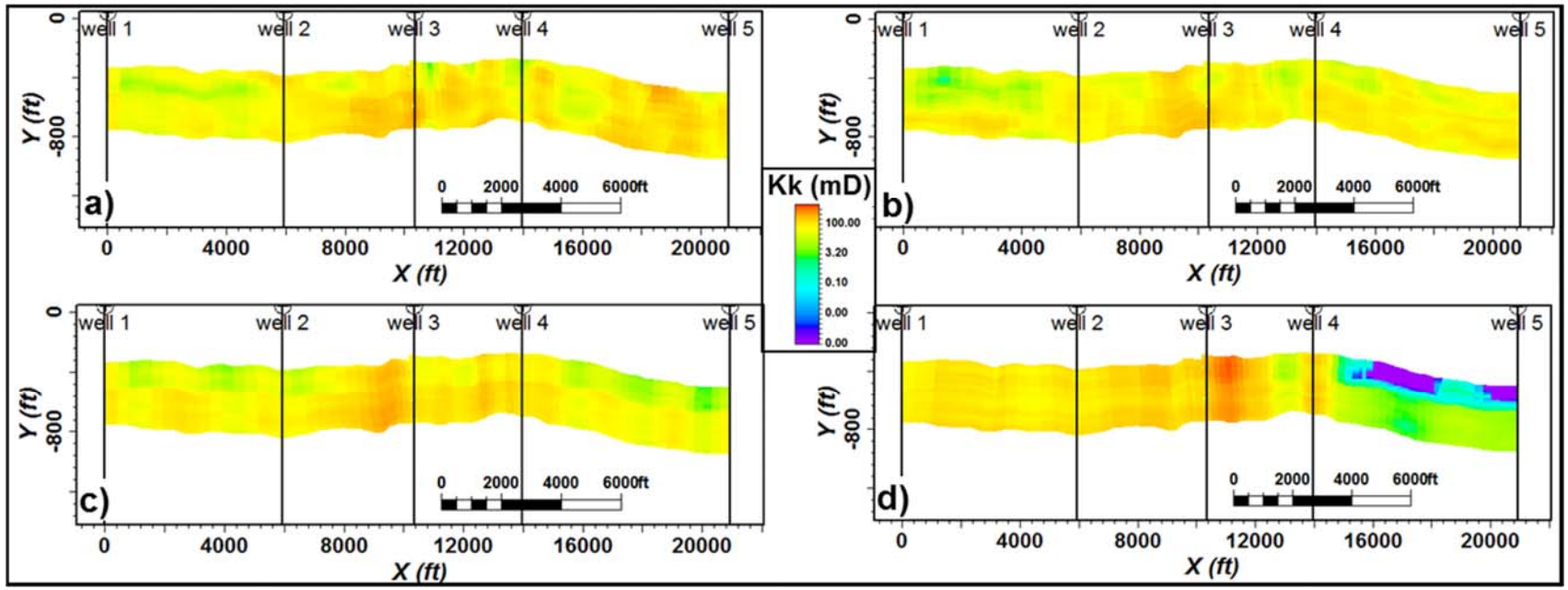

Figure 40. *The cross sections along five pseudo wells shown in figure 24 for the models guided by seismic attributes: a) amplitude contrast, b) chaos, c) curvature and d) consistent dip.*

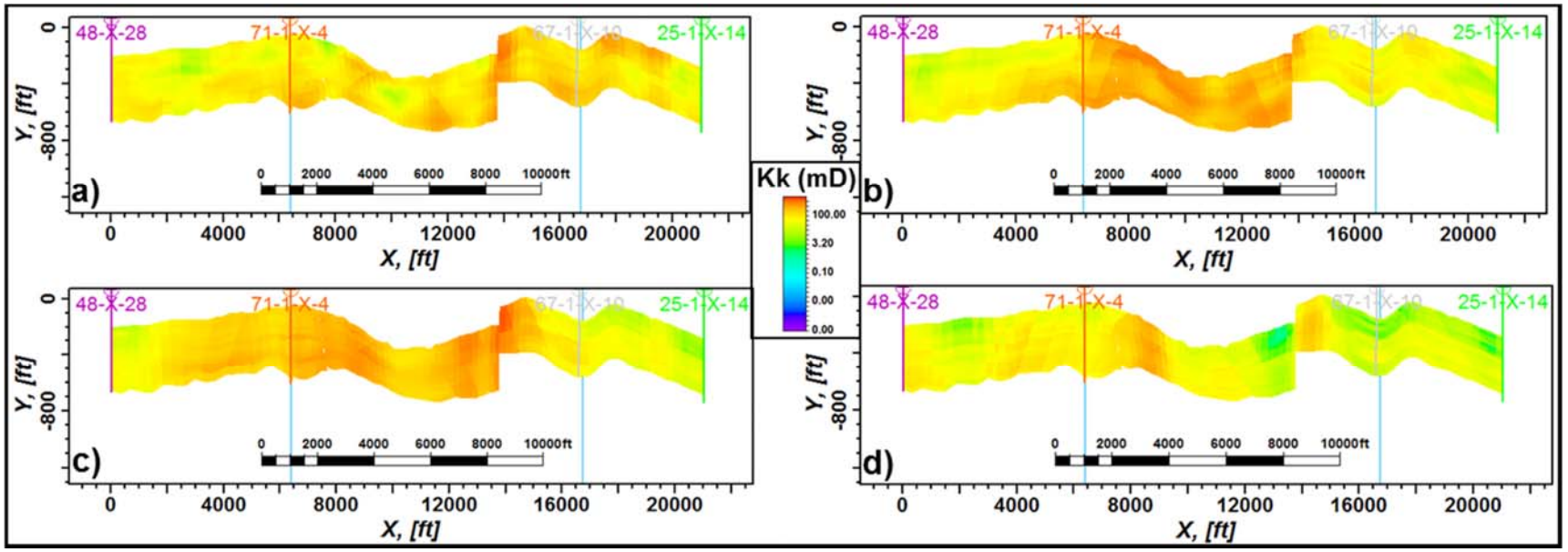

Figure 41. *The cross sections along the provided wells shown in figure 24 for the models guided by the seismic attributes: a) amplitude contrast, b) chaos, c) curvature and d) consistent dip.*

The cross sections based on the chaos and curvature attributes (Figure 41b, c) show extended high permeability zones mainly between the wells 71-1-x-4 and 67-1-x-10 along the fold hinge. The models displayed in Figure 41a and d, deliver local zones of the high permeability. The connected volumes are examined for the wells 3, 4 and 5 (Figures 42-44), since they are located in areas that highlight similarities and dissimilarities of the permeability between the models. Again, the connected volumes are based on grid cells with a permeability higher than the P90 value of the fracture data.

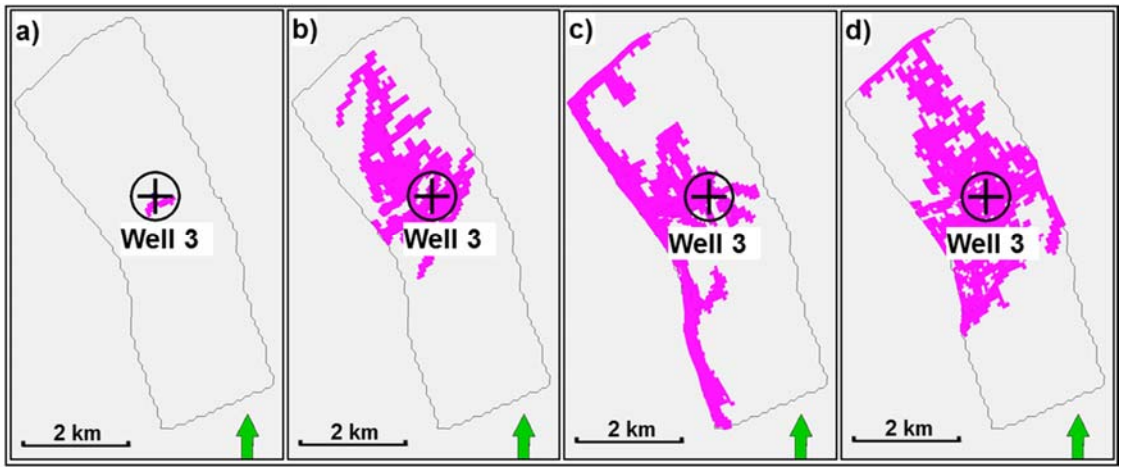

Figure 42. *Connected volumes for the pseudo well 3, for the models based on the seismic attributes: a) curvature, b) consistent dip, c) chaos and d) amplitude contrast.*

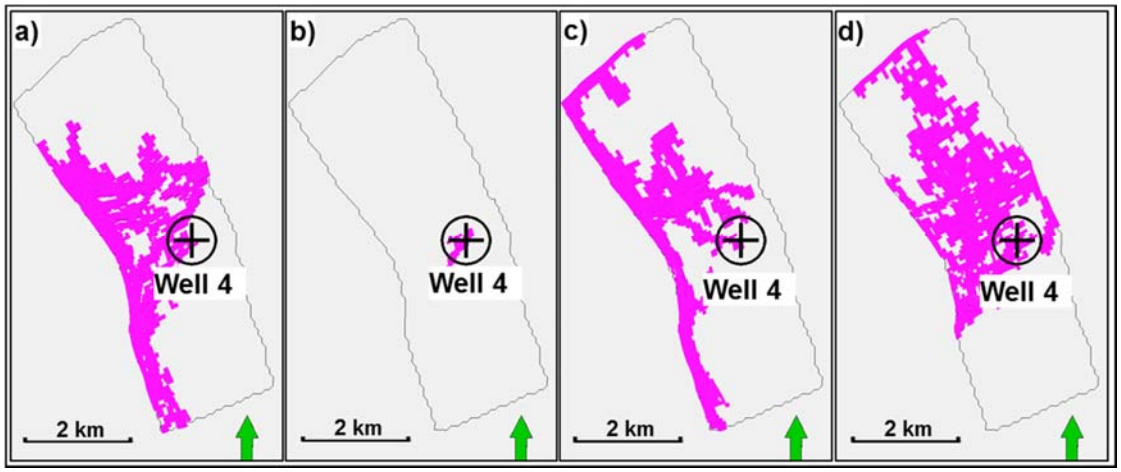

Figure 43. *Connected volumes for the pseudo well 4, for the models based on the seismic attributes: a) curvature, b) consistent dip, c) chaos and d) amplitude contrast.*

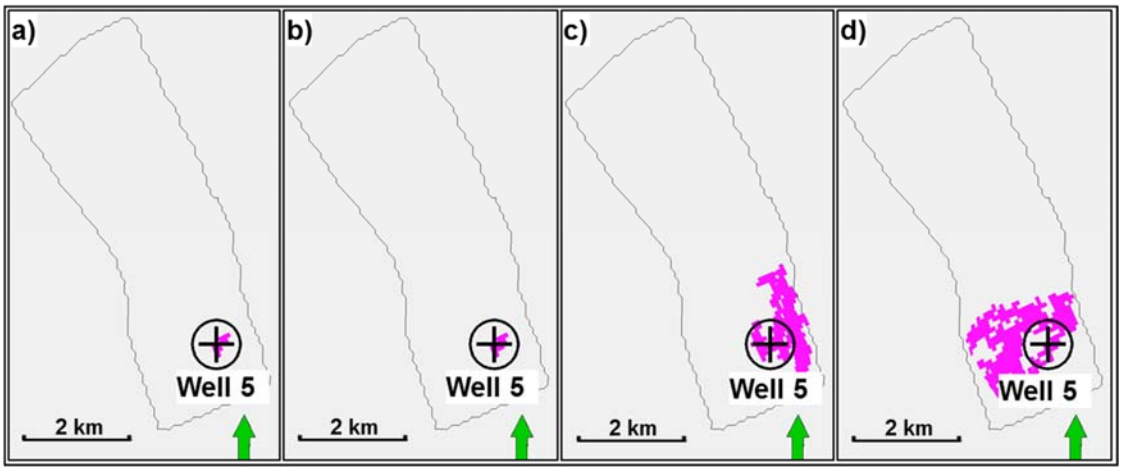

Figure 44. *Connected volumes for the pseudo well 5, for the models based on the seismic attributes: a) curvature, b) consistent dip, c) chaos and d) amplitude contrast.*

The similarities are mainly noticeable for the wells 3 and 4 of the models guided by chaos and amplitude contrast (Figures 42-43, c and d). The other two models (Figures 42-43, a and b) provide a surprisingly large difference between the two closely positioning wells 3 and 4. In addition, all models do not show an extension of the connectivity to the south of the well 4. While the models based on chaos and amplitude contrast deliver a considerable large area of the connected volumes linked to the well 5 (Figure 44, c and d), the models guided by the curvature and consistent dip do not show connected volumes of high permeability (Figure 44, a and b).

5.5 Discussion

5.5.1 Fracture intensity

The limited well data does not allow deriving a reliable fracture intensity property by Kriging or Gauss simulation. The variogram range used by the two interpolation techniques determines the radius of influence of the data points. Unfortunately, the horizontal variogram range is not known because of lack of well data. This underlines the uncertainty linked to the modeled fracture intensity and consequently to the resulting fracture model. The advantage of Gauss simulation lies in its ability to derive several equi-probable models that can be used for capturing the uncertainty of the fracture intensity distribution. The results seem to be more reliable compared to the Kriging in the sense that the distribution of the input data is honored. However, due to

the limited number of well data, the simulated fracture intensity cannot provide accurate information about the locations of high and low fracture density.

Based on the assumption that a strong relation exists between fractures and faults seismic attributes are used for deriving the fault pattern. This information is further used for calculating the fracture intensity models. Unfortunately, the seismic attributes analyzed in this study deliver fault patterns that deviate from each other. Consequently, the resultant fracture models are again subject to large uncertainty. However, the uncertainty in the horizontal variogram range can be addressed through deriving the variogram model from the seismic attributes. This workflow is justified under the assumption that the fractures and the faults are related to each other. Note that the vertical variogram range cannot be derived from the seismic attributes because of their low vertical resolution. Comparing the variogram models of the four seismic attributes, one can observe that consistent dip delivers a much larger horizontal variogram range compared to the other three attributes. This support the observation that the fracture intensity derived from the consistent dip attribute deviates considerably from the other three fracture intensity models. Consequently, the fracture model based on consistent dip should be regarded as an extreme case model.

5.5.2 Model parameters

The limited well data prevents an accurate modeling of the fracture properties. Therefore, in order to estimate and model the fracture properties, analogue studies are used. Statistical laws can be used to approximate the data from analogues. Numerous studies performed on different scales (from micro m to km) illustrate that the fracture length often follows a power law distribution. This is confirmed for the study area of this thesis. Therefore, all models incorporate the fracture length modeled by the power law with a shape factor of 2.8, a scale factor of 40 ft (13 m) and a maximum fracture length of 500 ft (150 m).

The differences of the dominant fracture orientation with respect to the different stratigraphic layers were discussed previously (see chapter 2, Geologic setting, section 2.3). The dominant fracture set at reservoir level is represented by the oblique striking fractures, but in addition, all models incorporate the fractures normal and parallel fractures to the hinge. The sensitivity analyses demonstrate that the key

parameter influencing the permeability is the fracture aperture (Figure 30). The aperture is related to the fracture length by the square root law (Figure 31). The calculation of the permeability from the aperture based on the cubic law delivers values that are in conflict with published data for the study area. In order to match the published permeability, a scaling factor is derived for the base case aperture. This scaling factor is also applied to the high case and low case in order to get an average permeability that is not in conflict with published data. The sensitivity analysis demonstrates that fracture length and orientation affect the upscaled permeability to a smaller degree than the aperture.

5.5.3 Comparison of the models

The comparison of the fracture models is challenging. The large number of fractures suggest analyzing the upscaled permeability derived from the fractures, because it is most influential on the reservoir performance. The simple comparison of statistical parameters turns out to be of limited help, because it does not take into account the size of high permeability zones or areas of "low flow". Therefore, the connected volumes defined by high permeability are chosen for comparing the derived models. Fracture models based on Kriging deliver very smooth permeability models. In contrast, models based on Gauss simulation give highly heterogeneous permeability models. Consequently, both types of models should show very different dynamic behavior, which could be studied for instance using flow line simulations. The models based on seismic attributes deliver a permeability pattern similar to the fault pattern because of the chosen high correlation coefficient between the fracture intensity and the seismic attributes. As the seismic attributes display fault patterns that differ on the local scale, they provide fracture models, which show very different connected high permeability bodies for the same wells in some areas. It can be expected that seismic attributes will deliver more consistent results when applied to modern high-resolution 3D seismic datasets.

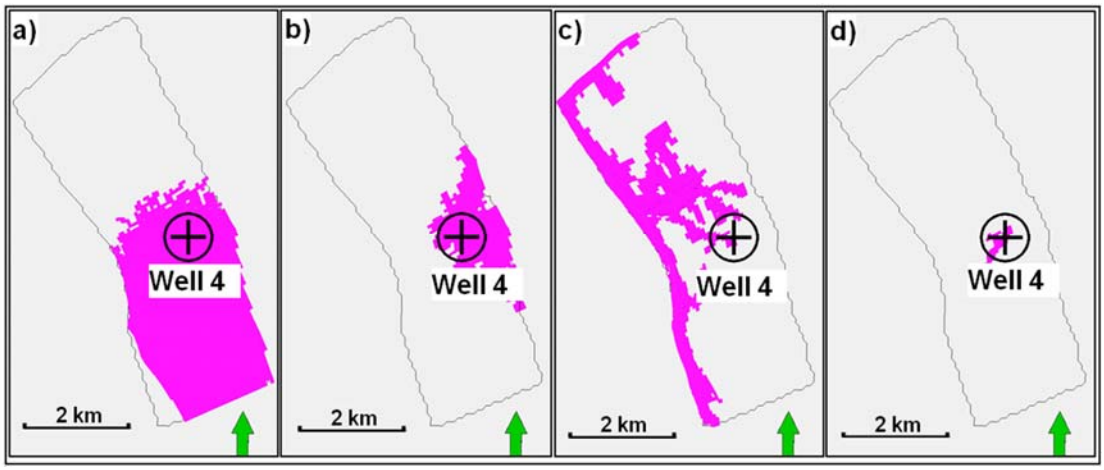

Figure 45. *Connected volumes for the pseudo well 4, for the models based on the different methods: a) Kriging, b) Gauss simulation, c) chaos attribute and d) consistent dip.*

Figure 45 summarizes the large uncertainty in fracture modeling for this dataset. It shows the connected volumes for the models based on Kriging, Gauss simulation and two seismic attributes. The significantly different pattern of the connected volumes linked to well 4 underlines the necessity of broad-band seismic with superior signal-noise ratio to guide the fracture modeling process.

6. Conclusion

The fracture modeling based on the dataset of the Teapot Dome reveals several conclusions:

- The main controlling factors of the fracture models are fracture intensity and aperture. While the fracture intensity controls the spatial permeability distribution, the fracture aperture represents the parameter that has the greatest influence on the absolute value of the permeability.
- The models based on Kriging and Gauss simulation do not deliver results and spatial permeability distribution in accordance with the observed fault and fold structures. Even though the algorithms deliver a permeability distribution comparable to the models based on seismic attributes, the spatial distribution and connectivity of high permeability zones are subject to high uncertainty.
- The models guided by the seismic attributes deliver a more reliable spatial permeability distribution illustrated by the zones of higher permeability located along the anticline and in the vicinity of the faults.
- Although the models deliver a similar permeability distribution, they show differences associated with the spatial distribution of the high permeability zones. Hence, the seismic guided fracture modeling requires special vigilance and control, since a model based on only one attribute can result in a questionable spatial permeability distribution.

Future work might consider the application of an alternative upscaling method (i.e. flow based method) with the aim of deriving the permeability models more accurately from the simulated fractures. Most importantly, production data would greatly enhance the reliability of fracture models. History matching is an excellent approach for the additional evaluation and uncertainty assessment of the models. Finally, the proposed methodology should be applied to modern high-resolution datasets in order to reduce the fracture model differences introduced by seismic attributes.

7. References

Anees, M., 2013. Seismic Attribute Analysis for Reservoir Characterization, 10 th Biennial International Conference and Exposition.

Aqrawi, A.A., Weinzierl, W., Daber, R. and Boe, T.H., 2012. SIS Norway Technology Center, 2Schlumberger Stavanger Research.

Baytok, S., 2010. Seismic investigation and attribute analysis of faults and fractures within a tight-gas sandstone reservoir: Williams Fork Formation, Mamm Creek Field, Piceance Basin, Colorado.

Bird, P., 1998. Kinematic history of the Laramide orogeny in latitudes 35o-49oN, western United States. Tectonics, 17(5): 780-801.

Bohling, G., 2005. Introduction to geostatistics and variogram analysis. Kansas geological survey, 2.

Chiaramonte, L., 2009. Geomechanical Characterization and Reservoir Simulation of a Carbon Dioxide Sequestration Project in a Mature Oil Field, Teapot Dome, WY. ProQuest.

Chopra, S. and Marfurt, K.J., 2007. Seismic attributes for prospect identification and reservoir characterization.

Cooper, S., 2000. Deformation within a basement-cored anticline Teapot Dome. Wyoming [MS thesis]: New Mexico Institute of Mining and Technology, 274.

Cooper, S.P., Goodwin, L.B. and Lorenz, J.C., 2006. Fracture and fault patterns associated with basement-cored anticlines: The example of Teapot Dome, Wyoming. AAPG bulletin, 90(12): 1903-1920.

Cooper, S.P., Hart, B., Lorenz, J.C., Goodwin, L.B. and Milliken, M., 2003. Outcrop and seismic analysis of natural fractures, faults and structure at Teapot Dome, Wyoming.

Cowie, P.A. and Scholz, C.H., 1992. Physical explanation for the displacement-length relationship of faults using a post-yield fracture mechanics model. Journal of Structural Geology, 14(10): 1133-1148.

Davis, J.C. and Sampson, R.J., 1986. Statistics and data analysis in geology, 646. Wiley New York et al.

Decroux, B. and Gosselin, O., 2013. Computation of effective dynamic properties of naturally fractured reservoirs: Comparison and validation of methods, EAGE Annual Conference & Exhibition incorporating SPE Europec. Society of Petroleum Engineers.

Dershowitz, W.S. and Herda, H.H., 1992. Interpretation of fracture spacing and intensity, The 33th US Symposium on Rock Mechanics (USRMS). American Rock Mechanics Association.

Dickinson, W.R., Klute, M.A., Hayes, M.J., Janecke, S.U., Lundin, E.R., McKITTRICK, M.A. and Olivares, M.D., 1988. Paleogeographic and paleotectonic setting of Laramide sedimentary basins in the central Rocky Mountain region. Geological Society of America Bulletin, 100(7): 1023-1039.

Dickinson, W.R. and Snyder, W.S., 1978. Plate tectonics of the Laramide orogeny. Geological Society of America Memoirs, 151: 355-366.

Doelger, M. and Mullen, D., Barlow & Haun, I., 1993. Nearshore marine sandstone, Atlas of Major Rocky Mountain Gas Reservoirs: Socorro, NM, New Mexico Bureau of Mines and Mineral Resources: 54-55.

Doll, T., Luers, D., Strong, G., Schulte, R., Sarathi, P., Olsen, D. and Hendricks, M., 1995. An update of steam injection operations at Naval Petroleum Reserve No. 3, Teapot Dome Field, Wyoming: A shallow heterogeneous light oil reservoir, SPE International Heavy Oil Symposium. Society of Petroleum Engineers.

El Ouahed, A.K., Tiab, D. and Mazouzi, A., 2005. Application of artificial intelligence to characterize naturally fractured zones in Hassi Messaoud Oil Field, Algeria. Journal of Petroleum Science and Engineering, 49(3): 122-141.

Fossen, H., 2010. Structural geology. Cambridge University Press.

Fox, J., Dolton, G. and Clayton, J., 1991. Powder River Basin. Economic Geology, US: Geological Society of America, The Geology of North America, P-2: 373-390.

Friedmann, S., Nummedal, D. and Stamp, V., 2004. Science and technology goals of the Teapot Dome field experimental facility, National Energy Technology Laboratory 3rd Annual Carbon Sequestration Conference Proceedings: Alexandria, Virginia, Exchange Monitor Publications.

Friedmann, S.J. and Stamp, V.W., 2006. Teapot Dome: Characterization of a CO2-enhanced oil recovery and storage site in Eastern Wyoming. Environmental Geosciences, 13(3): 181-199.

Gao, D., Wilson, T., Zhu, L. and Marfurt, K.J., 2011. 3D seismic curvature and flexure for unconventional fractured reservoir characterization at Teapot Dome (Wyoming), 2011 SEG Annual Meeting. Society of Exploration Geophysicists.

Garrett, C. and Lorenz, J., 1990. Fracturing along the Grand Hogback, Garfield County, Colorado, New Mexico Geological Society Guidebook, 41st Field Conference, Southern Sangre de Cristo Mountains, New Mexico, pp. 145-150.

Gay, S., 1999. An Explanation for" 4-Way Closure" of Thrust-Fold Structures in the Rocky Mountains, and Implications for Similar Structures Elsewhere. MOUNTAIN GEOLOGIST, 36: 235-244.

Gilbertson, N. and Hurley, N., 2006. 3-D geologic modeling and fracture interpretation of the Tensleep Sandstone. Alcova anticline, Wyoming: MS thesis, Colorado School of Mines, Golden.

Hart, B.S., Pearson, R. and Rawling, G.C., 2002. 3-D seismic horizon-based approaches to fracture-swarm sweet spot definition in tight-gas reservoirs. The Leading Edge, 21(1): 28-35.

Hennings, P., Olson, J. and Thompson, L., 1998. Using outcrop data to calibrate 3-D geometric models for prediction of reservoir-scale deformation: An example from Wyoming, Fractured reservoirs: practical exploration and development strategies, Symposium Proceedings, pp. 91-95.

Joonnekindt, J., Legrand, X., Lee, B., Lefranc, M., Maerten, L. and Anis, L., 2013. Innovative Natural Fracture Prediction using a Geomechanically-Based Solution: Application to the Malay Basin (Malaysia), Second EAGE Workshop on Naturally Fractured Reservoirs.

Klein, P., Richard, L. and James, H., 2008. 3D curvature attributes: a new approach for seismic interpretation. First break, 26(4).

Klimczak, C., Schultz, R.A., Parashar, R. and Reeves, D.M., 2010. Cubic law with aperture-length correlation: implications for network scale fluid flow. Hydrogeology Journal, 18(4): 851-862.

La Pointe, P.R., Hermanson, J. and Eiben, T., 2002. 3-D reservoir and stochastic fracture network modeling for enhanced oil recovery, Circle r\ Ridge Phosphoria/Tensleep reservoir, Wind River Reservation, Arapaho and Shoshone tribes, Wyoming, Wyoming: Final Technical Report, May 1, 2000 through October 31, 2002, DOE Award Number: DE-FG26-00BC15190.

Lee, C.-C., Lee, C.-H., Yeh, H.-F. and Lin, H.-I., 2011. Modeling spatial fracture intensity as a control on flow in fractured rock. Environmental Earth Sciences, 63(6): 1199-1211.

Lefranc, M., Farag, S., Souche, L. and Dubois, A., 2012. Fractured Basement Reservoir Characterization for Fracture Distribution, Porosity and Permeability Prediction, AAPG International Conference and Exhibition, Singapore, pp. 16-19.

Li, Y., 2014. An Uncertainty Analysis of Modeling Geologic Carbon Sequestration in a Naturally Fractured Reservoir at Teapot Dome, Wyoming. University of Wyoming.

Lorenz, J.C. and Cooper, S.P., 2013. Natural fractures in folded sandstones of the Tensleep Formation, Wyoming.

Lorenz, J.C. and Hill, R.E., 1992. SAND91-0281C.

Marfurt, K.J. and Chopra, S., 2006. Seismic attribute mapping of structure and stratigraphy.

McCutcheon, T., 2003. Time structure maps–3D seismic data interpretation, Teapot Dome Oil Field, Naval Petroleum Reserve No. 3, Natrona County, Wyoming. Rocky Mountain Oilfield testing center report.

Milliken, M. and Koepsell, R., 2003. Imaging Technology offers enhanced interpretation of Teapot Dome reservoirs.

Nelson, R., 2001. Geologic analysis of naturally fractured reservoirs. Gulf Professional Publishing.

Olson, J.E., 2003. Sublinear scaling of fracture aperture versus length: an exception or the rule? Journal of Geophysical Research: Solid Earth, 108(B9).

Ortega, O.J., Marrett, R.A. and Laubach, S.E., 2006. A scale-independent approach to fracture intensity and average spacing measurement. AAPG bulletin, 90(2): 193-208.

Ortega Pérez, O.J., 2002. Fracture-size scaling and stratigraphic controls on fracture intensity. Dissertation Thesis, University of Texas at Austin.

Ouenes, A., 2000. Practical application of fuzzy logic and neural networks to fractured reservoir characterization. Computers & Geosciences, 26(8): 953-962.

Ouenes, A., Anderson, T.C., Klepacki, D., Bachir, A., Boukhelf, D., Robinson, G.C., Holmes, M., Black, B.J. and Stamp, V.W., 2010. Integrated characterization and simulation of the fractured Tensleep Reservoir at Teapot Dome for CO2 injection design, SPE Western Regional Meeting. Society of Petroleum Engineers.

Ouenes, A. and Hartley, L.J., 2000. Integrated fractured reservoir modeling using both discrete and continuum approaches, SPE Annual Technical Conference and Exhibition. Society of Petroleum Engineers.

Ouenes, A., Richardson, S. and Weiss, W., 1995. Fractured reservoir characterization and performance forecasting using geomechanics and artificial intelligence, SPE Annual Technical Conference and Exhibition. Society of Petroleum Engineers.

Pedersen, S.I., Randen, T., Sonneland, L. and Steen, O., 2002. Automatic 3D fault interpretation by artificial ants, 64th EAGE Conference & Exhibition.

Phillips, H., Joonnekindt, J. and Maerten, L., 2014. Natural Fracture Prediction for Discrete Fracture Modelling, 76th EAGE Conference and Exhibition 2014.

Randen, T., Pedersen, S.I. and Sonneland, L., 2001. Automatic extraction of fault surfaces from three-dimensional seismic data, Annual International Meeting, Society Exploration Geophycist, Expanded abstract.

Randen, T., Sønneland, L., Carrillat, A., Valen, T., Skov, T., Pedersen, S., Rafaelsen, B. and Elvebakk, G., 2003. Preconditioning for optimal 3d stratigraphical and structural inversion, 65th EAGE Conference & Exhibition.

Ringrose, P. and Bentley, M., 2015. Reservoir model design. Springer.

RMOTC, 2005a. Teapot Dome, Natrona County, Wyoming, NPR-3, well data set, CD-ROM. RMOTC (Rocky Mountain Oilfield Testing Center).

RMOTC, 2005b. Teapot Dome, Natrona County, Wyoming, 2D and 3D seismic data set, CD-ROM. RMOTC (Rocky Mountain Oilfield Testing Center).

Roberts, A., 2001. Curvature attributes and their application to 3 D interpreted horizons. First break, 19(2): 85-100.

Schlumberger, 2013. Fracture Modeling Course, Training and Exercise Guide. Schlumberger, pp. 474.

Scholz, C.H., 2002. The mechanics of earthquakes and faulting. Cambridge university press.

Schwartz, B.C., 2006. Fracture pattern characterization of the Tensleep Formation, Teapot Dome, Wyoming, West Virginia University.

Shen, F. and Ouenes, A., 2003. Seismically driven integrated fracture modeling, SPE Annual Technical Conference and Exhibition. Society of Petroleum Engineers.

Smith, V.L., 2008. Modeling natural fracture networks: Establishing the groundwork for flow simulation at Teapot Dome, Wyoming. WEST VIRGINIA UNIVERSITY.

Snow, D.T., 1969. Anisotropie permeability of fractured media. Water Resources Research, 5(6): 1273-1289.

Stearns, D.W. and Friedman, M., 1972. Reservoirs in fractured rock: Geologic exploration methods.

Stone, D.S., 1993. Basement-involved thrust-generated folds as seismically imaged in the subsurface of the central Rocky Mountain foreland. Geological Society of America Special Papers, 280: 271-318.

Thachaparambil, M.V., 2015. Discrete 3D fracture network extraction and characterization from 3D seismic data—A case study at Teapot Dome. Interpretation, 3(3): ST29-ST41.

van der Most, M., 2008. The analysis of directional permeability of fractured reservoirs: A case study from the Tata area, Morocco, Master's thesis, Delft University of Technology, Netherlands.

Vermilye, J.M. and Scholz, C.H., 1995. Relation between vein length and aperture. Journal of Structural Geology, 17(3): 423-434.

Wilson, T.H., Smith, V. and Brown, A., 2013. Developing a strategy for CO 2 EOR in an unconventional reservoir using 3D seismic attribute workflows and fracture image logs, 2013 SEG Annual Meeting. Society of Exploration Geophysicists.

Wilson, T.H., Smith, V. and Brown, A., 2015. Developing a model discrete fracture network, drilling, and enhanced oil recovery strategy in an unconventional naturally fractured reservoir using integrated field, image log, and three-dimensional seismic data. AAPG Bulletin, 99(4): 735-762.

Witherspoon, P.A., Wang, J., Iwai, K. and Gale, J., 1980. Validity of cubic law for fluid flow in a deformable rock fracture. Water resources research, 16(6): 1016-1024.

Zellou, A.M., Ouenes, A. and Banik, A., 1995. Improved fractured reservoir characterization using neural networks, geomechanics and 3-D seismic, SPE Annual Technical Conference and Exhibition. Society of Petroleum Engineers.

Zhang, Q., 2007. Stratigraphy and sedimentology of the Tensleep Sandstone at the Teapot dome and in outcrops. Wyoming: MS thesis, University of Wyoming, Laramie.